Two-dimensional-lattice-confined single-molecule-like aggregates

https://doi.org/10.1038/s41586-024-07925-9

Received: 3 October 2023

Accepted: 8 August 2024

Published online: 11 September 2024



Check for updates

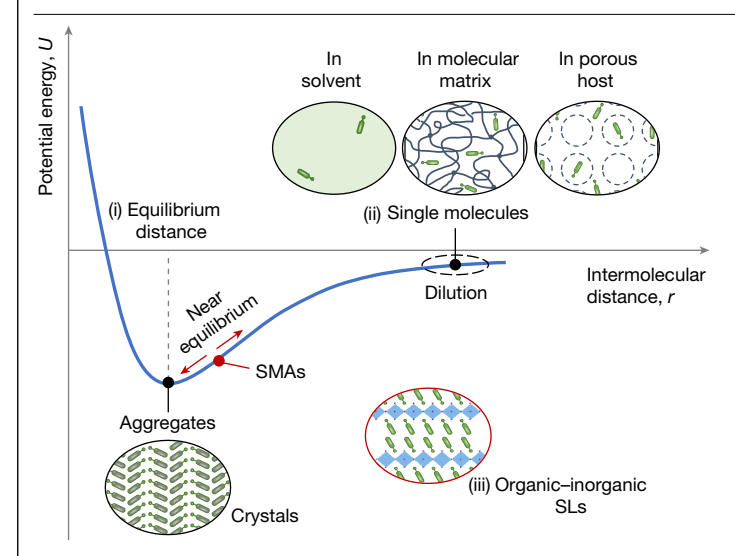
Kang Wang^{1,2}, Zih-Yu Lin¹, Angana De³, Conrad A. Kocoj^{4,5}, Wenhao Shao¹, Hanjun Yang^{1,3}, Zehua He², Aidan H. Coffey⁶, Colton B. Fruhling^{7,8}, Yuanhao Tang¹, Dharini Varadharajan¹, Chenhui Zhu⁶, Yong Sheng Zhao², Alexandra Boltasseva^{7,8}, Vladimir M. Shalaev^{7,8}, Peijun Guo^{4,5}, Brett M. Savoie^{1™} & Letian Dou^{1,3,8™}

Intermolecular distance largely determines the optoelectronic properties of organic matter. Conventional organic luminescent molecules are commonly used either as aggregates or as single molecules that are diluted in a foreigner matrix. They have garnered great research interest in recent decades for a variety of applications, including light-emitting diodes^{1,2}, lasers³⁻⁵ and quantum technologies^{6,7}, among others⁸⁻¹⁰. However, there is still a knowledge gap on how these molecules behave between the aggregation and dilution states. Here we report an unprecedented phase of molecular aggregate that forms in a two-dimensional hybrid perovskite superlattice with a near-equilibrium distance, which we refer to as a single-molecule-like aggregate (SMA). By implementing two-dimensional superlattices, the organic emitters are held in proximity, but, surprisingly, remain electronically isolated, thereby resulting in a near-unity photoluminescence quantum yield, akin to that of single molecules. Moreover, the emitters within the perovskite superlattices demonstrate strong alignment and dense packing resembling aggregates, allowing for the observation of robust directional emission, substantially enhanced radiative recombination and efficient lasing. Molecular dynamics simulations together with single-crystal structure analysis emphasize the critical role of the internal rotational and vibrational degrees of freedom of the molecules in the two-dimensional lattice for creating the exclusive SMA phase. This two-dimensional superlattice unifies the paradoxical properties of single molecules and aggregates, thus offering exciting possibilities for advanced spectroscopic and photonic applications.

Organic crystals that demonstrate an intermolecular distance at the equilibrium point (3-5 Å; Fig. 1(i)) are one of the most stable aggregated phases. In this equilibrium state, organic molecules generally exhibit strong intermolecular interactions (for example, π – π stacking, energy transfer, charge transfer and self-absorption), which result in a notable drop in their photoluminescence quantum yield (PLQY)¹¹. This phenomenon is widely known as aggregation-caused quenching (ACQ), which is a substantial restriction for the practical use of aggregated emitters. An effective strategy to alleviate ACQ was to weaken or eliminate intermolecular interactions by spatially disengaging the emitters far away from each other (>10 Å; Fig. 1(ii)), such as by dissolving them in solvents, diluting them in a foreigner matrix 12-14, embedding them into porous hosts¹⁵⁻¹⁷ or growing macrocycle-hostsbased supramolecular single crystals^{18,19}. These well-isolated single molecules have allowed efficient emission and set the foundation for organic light-emitting diodes^{2,20}, lasers and many other optoelectronic applications. Nonetheless, scarce reports exist on organic emitters with an intermolecular distance between the equilibrium and dilution states and their behaviours have received limited research attention.

Two-dimensional (2D) layered hybrid perovskites are emerging solution-processable semiconducting materials, combining the advantages of both organic and inorganic components²¹⁻²⁵. These unique 2D organic-inorganic superlattices (SLs) offer a platform to investigate the behaviours of organic emitters near the equilibrium state because the inorganic sheets intrinsically demonstrate a square lattice with an approximately 6-Å pitch to house organic molecules (Fig. 1(iii)), which is potentially sufficient to modulate or suppress intermolecular interactions. Numerous studies have been focusing on how the incorporation of organic moieties improves the luminescent efficiency²⁶, $charge-transport\, capability^{27}\, and\, stability^{22,27,28}\, of inorganic\, slabs, which$ have led to many breakthroughs in high-performance perovskite electronic and optoelectronic devices²⁹⁻³³. However, making use of the inorganic sublattice to tune the intermolecular interactions, molecular packing and emission properties of organic molecules remains largely unexplored. Starting from the late 1990s, several groups have reported

Davidson School of Chemical Engineering, Purdue University, West Lafayette, IN, USA. 2Key Laboratory of Photochemistry, Institute of Chemistry, Chinese Academy of Sciences, Beijing, China. 3Department of Chemistry, Purdue University, West Lafavette, IN, USA, 4Department of Chemical & Environmental Engineering, Yale University, New Hayen, CT, USA, 5Energy Sciences Institute, Yale University, West Haven, CT, USA. 6 Advanced Light Source, Lawrence Berkeley National Laboratory, Berkeley, CA, USA. 7 Elmore Family School of Electrical and Computer Engineering, Purdue University, West Lafayette, IN, USA. Birck Nanotechnology Center, Purdue University, West Lafayette, IN, USA. e-mail: bsavoie@purdue.edu; dou10@purdue.edu



 $\label{eq:Fig.1} \textbf{Fig. 1} | \textbf{Schematic illustration for different scenarios of molecular emitters with varying intermolecular distances.} \ (i) \ Equilibrium state. The intermolecular distance in organic crystals is typically within 3–5 Å, which enables the lowest potential energy. This can be considered as the equilibrium state with aggregate behaviour. (ii) Dilution state. The molecules are separated far away from each other (>10 Å), leading to a dilution state with single-molecule behaviour. (iii) Near-equilibrium state. Organic emitters, confined in organic-inorganic 2D SLs with an intermolecular distance near the equilibrium state, behave as single molecules but also deliver some aggregate properties, thus being termed SMAs.$

the formation of organic semiconductor–perovskite SLs and confirmed that the emitting species could be organic chromophores $^{22,34-37}$. However, the range of organic molecular emitters that can be incorporated into layered perovskites is rather limited and their PLQYs are often low (typically below 10%).

In this study, we demonstrate a new phase of molecular aggregates, which we refer to as a SMA, that was achieved near the equilibrium state by combining a 2D inorganic sublattice with suitably tailored organic chromophores. In this hybrid SL, the behaviour of organic emitters closely resembles that of individual single molecules, as evidenced by their similar emission wavelengths and lifetimes, as well as near-unity PLQYs. Theoretical and experimental investigations highlight the pivotal role of backbone dihedrals of the organic emitter in maintaining this single-molecule behaviour. Notably, despite exhibiting single-molecule-like properties, the strong alignment and close packing of organic molecules within the 2D SLs resulted in intense directional emission, ultrafast radiative recombination and efficient lasing, which are linked to the traits of ordered molecular ensembles or aggregates.

SMA materials design

We designed and synthesized two new organic molecular emitters, 2-(5-(7-(9,9-dimethyl-9H-fluoren-2-yl)benzo[c][1,2,5]thiadiazol-4-yl) thiophen-2-yl)ethan-1-ammonium bromide (referred to as FBTT; Fig. 2a) and 2-(4-(7-(9,9-dimethyl-9H-fluoren-2-yl)benzo[c][1,2,5] thiadiazol-4-yl)phenyl)ethan-1-ammonium bromide (referred to as FBTP; Fig. 2e), and incorporated them into the 2D perovskite lattices. The synthetic procedures of the organic molecules are detailed in the Supplementary Information (Supplementary Figs. 1–4). The chromophore core was adapted from the repeating unit of a bright-green-emitting polymer, poly(9,9-dioctylfluorene-*alt*-benzothiadiazole) (F8BT) 38 . The alkyl chain length was cut to one carbon to ensure that they can be accommodated in the perovskite lattice. Linkers, such as thienyl and phenyl groups, were further introduced to connect the chromophore

core with the ammonium tail and then ionically bonded with the lead halide matrix.

Lead bromide was selected as the inorganic framework to construct a reversed type-I band alignment for organic compounds to emit efficiently³⁹, which is confirmed by density functional theory (DFT) and time-dependent density functional theory (TDDFT) simulations (Extended Data Fig. 1). We then carried out thin-film studies on the aggregates (neat organic emitters), 2D SLs (organic-emitter-incorporated perovskites) and isolated monomers (2 wt% organic emitters doped poly(methyl methacrylate) (PMMA) films). Grazing-incidence wide-angle X-ray scattering (GIWAXS) and X-ray diffraction (XRD) characterizations helped us verify that both FBTT and FBTP were successfully incorporated, forming a layered perovskite structure (Fig. 2b.f. Extended Data Fig. 2 and Supplementary Fig. 5). The sharp ultraviolet-visible (UV-vis) peak around 400 nm and the nearby shoulder peak from 2D SL films (Supplementary Fig. 5) can be indexed to the excitonic peak of perovskites and organic emitters, respectively, further supporting the formation of 2D perovskites.

The PL spectrum of FBTT SLs (peaked at about 594 nm; Fig. 2c) is similar to that of its aggregates and redshifted compared with its monomer state (PL peak at 559 nm). This redshift is usually ascribed to the intermolecular interaction, especially π – π stacking, induced bandgap narrowing. Notably, by contrast, the PL spectrum of FBTP SLs (peaked at about 540 nm; Fig. 2g) is similar to the FBTP monomers and clearly blueshifted compared with the aggregates (peaked at 553 nm). The inset PL images in Fig. 2c,g further support the above results. The absence of perovskite emission (violet profiles in Fig. 2c,g) in both FBTT and FBTP SLs substantiates the fact that both 2D SLs are subject to a reversed type-I band alignment. Moreover, the FBTT SLs and aggregates seem to have a similar PLQY of about 15%, which is much lower than its monomer (81.2%). This can be explained by the notorious ACQ effect. Surprisingly, the ACQ effect is absent in the FBTP SLs sample, which features a much higher PLQY (92.8%) than that of its aggregates (42.4%). Such a high PLQY is very close to that of its monomers (PLQY = 95.7%). To the best of our knowledge, this is the highest PLQY reported so far for a 2D perovskite material^{22,26,35}. These results indicate that the FBTT molecules in perovskites behave more like aggregates, whereas the FBTP molecules in perovskites behave like single molecules.

Fluorescence lifetime imaging microscopy (FLIM) measurements show that FBTT SLs manifest similar PL lifetime as its aggregates (Fig. 2d), which is much shorter than that of the FBTT monomer, again validating the aggregation behaviour of FBTT in the perovskite SLs. The PL lifetime of FBTP SLs matches well with its monomer case (Fig. 2h). It should be noted that the pitch size of the inorganic square lattice can be fine-tuned by introducing different halides, such as Cl⁻ or I⁻, which would enable different behaviours of organic emitters. After mixing with I⁻, the inorganic sublattice will slightly expand and the inter-emitter distance will increase towards the dilution state. Consequently, the single-molecule behaviour is maintained, as evidenced by an identical PL emission peak (solid blue curve in Extended Data Fig. 3) to that of single molecules and the pure bromide case, whereas the incorporation of Cl- will constrain the inorganic sublattice and the organic emitter will be brought even closer towards the equilibrium state, thus leading to a similar PL emission as that of aggregates (solid brown and red curves in Extended Data Fig. 3). Furthermore, the FBTT and FBTP yielded 2D SL thin films exhibiting similar surface morphology and thickness (Extended Data Fig. 4, Supplementary Fig. 6 and Methods). Also, the emission spectra of single-crystalline 2D perovskite crystals derived from FBTT and FBTP resemble those of their corresponding polycrystalline thin films (Extended Data Fig. 5). These observations eliminate film quality and crystallinity as confounding factors governing the differential emission properties.

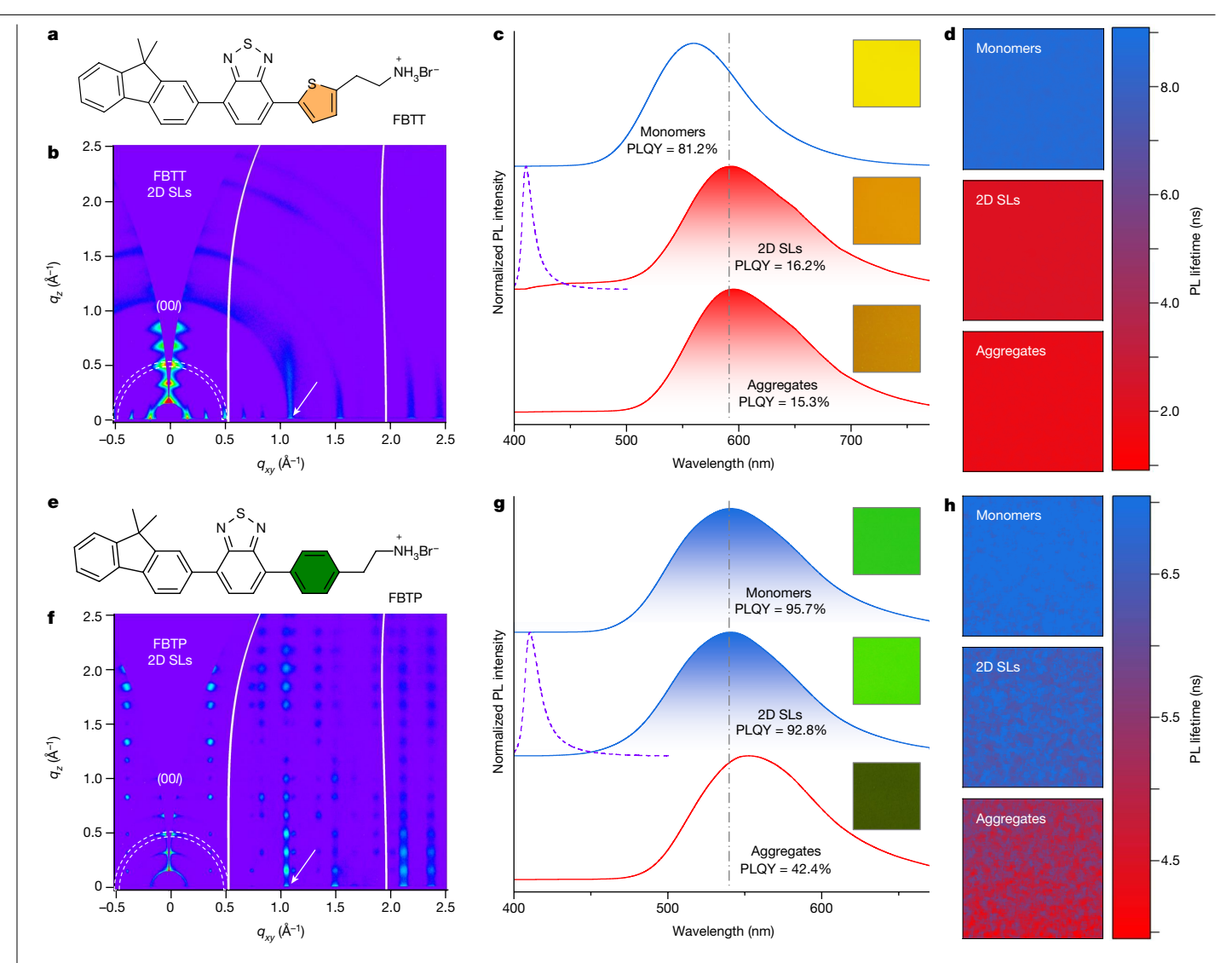


Fig. 2 | Single-molecule behaviour of molecular emitters in perovskite 2D SLs. a, Molecular structure of FBTT. b, GIWAXS pattern of FBTT 2D SL thin film, c.d. PL spectra and PLOY (c) and FLIM mapping (d) of FBTT monomer in PMMA, FBTT 2D SLs and FBTT aggregate films. e, Molecular structure of FBTP. f, GIWAXS pattern of FBTP 2D SL thin film. g,h, PL spectra and PLQY (g) and FLIM mapping (h) of FBTP monomer in PMMA, FBTP 2D SLs and FBTP aggregate films. Note that the colour scales in ${\bf b}$ and ${\bf f}$ are adjusted differently to effectively highlight the scattering along the q_{xy} direction; the dashed white rings highlight the scattering pattern at a typical q near 0.5 Å⁻¹ with their intensity shown in Extended Data Fig. 2; the solid white lines are blank spaces

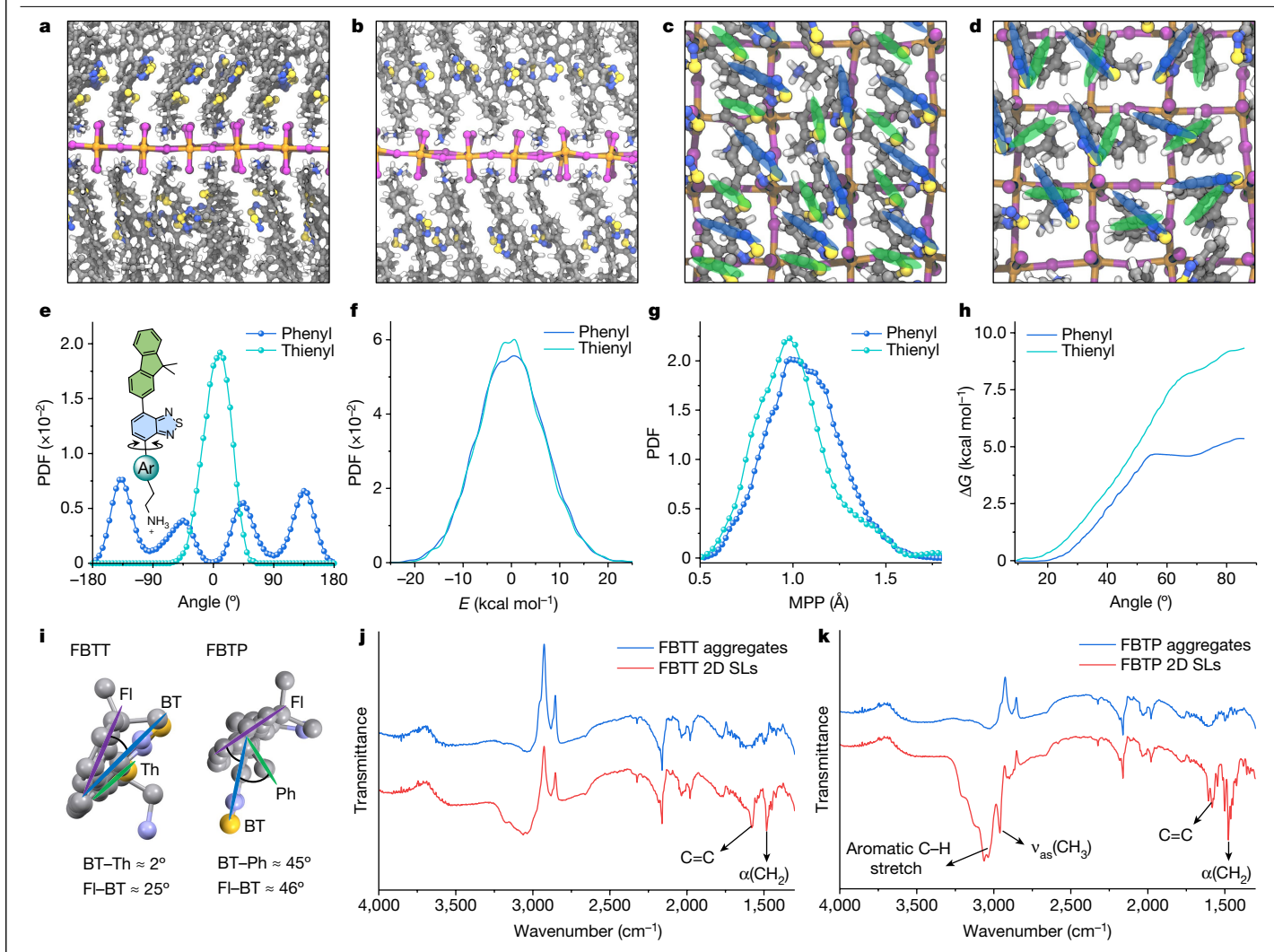
derived from the raw GIWAXS data, which are collected by splicing the detector images; and the white arrows indicate the (100) diffraction and confirm the 2D perovskite structure. The dashed violet curves in c and g are the PL spectra of (PEA)₂PbBr₄ (PEA is phenylethylammonium), which implies the emission feature of the 2D lead bromide lattice, and the grey dash-dot lines indicate the PL peaks of the 2D SLs compared with those of the monomers and aggregates. The insets are PL images of the corresponding thin-film samples and all the image scales are 10 μ m \times 10 μ m. The scales of all FLIM images in **d** and **h** are $50 \, \mu m \times 50 \, \mu m$.

Molecular insights

To understand the relationship between the emitter structures and their behaviours in the lattice, we performed equilibrium molecular dynamics (MD) simulations on individual FBTT-based and FBTP-based layered perovskites, following equilibration and statistical sampling over finite-temperature equilibrium structures (see Methods for simulation details). As shown in Fig. 3a,b, FBTT adopts a more ordered packing style than FBTP (side view in Supplementary Fig. 7). Further investigations on the configuration of each ligand reveal that FBTT ligands are more planar than FBTP, characterized by the fact that the benzothiadiazole and thienyl rings in FBTT ligands are parallel (Fig. 3c), whereas the benzothiadiazole and phenyl rings in FBTP are not (Fig. 3d). Co-planar molecules usually experience stronger intermolecular interactions, such as π - π stacking, that promote emission quenching and

wavelength redshifting, agreeing well with the experimental observations in FBTT.

To quantitatively understand the configuration and intermolecular interactions of the ligands, the distribution of the inter-ring dihedral, the site energy (calculated as a sum over all intermolecular terms involving the ligands) and the molecular planarity parameter (calculated as the root-mean-square deviation of atoms from the fitting plane to the ligand) of each ligand were calculated. All distribution data were collected from each frame of the MD trajectory based on different ligands. The simulations on the dihedral between fluorene and benzothiadiazole give similar distribution profiles for both FBTT and FBTP (Supplementary Fig. 8), whereas the dihedral torsions between benzothiadiazole and phenyl/thienyl rings are very different. As shown in Fig. 3e, FBTT manifests a narrow dihedral distribution converging around 0°, whereas the distribution of FBTP spreads out and peaked



 $\label{eq:Fig. 3} | \textbf{Molecular insights into the rotational and vibrational behaviours of organic molecules confined in 2D SLs. a, b, Side view of thienyl-based (a) and phenyl-based (b) 2D SLs during MD simulations. c, d, Top view of thienyl-based (c) and phenyl-based (d) 2D SLs during MD simulations. Fluorene units are omitted for clarity. e, Probability distribution function (PDF) of each ligand's backbone dihedral torsion between benzothiadiazole and the respective aromatic ring (Ar) in the perovskite lattice. f, The energy PDF of each ligand in the perovskite lattice. g, PDF of each ligand's molecular planarity parameter (MPP) in the perovskite lattice. h, Free energy for neighbouring ligand rotation in the perovskite lattice. i, Zoomed-in top-view images of FBTT (left) and FBTP$

(right) molecules extracted from their corresponding 2D SL single-crystal structures. Hydrogen atoms are omitted for clarity. In \mathbf{a} – \mathbf{d} , \mathbf{i} , blue lines denote benzothiadiazole (BT); green lines denote thienyl (Th) rings and phenyl (Ph) rings; purple denotes fluorene (Fl) units; blue spheres denote nitrogen, yellow spheres sulfur, pink and purple spheres bromine, orange spheres lead, and grey spheres carbon. \mathbf{j} , \mathbf{k} , FTIR of FBTT aggregates and 2D SL films (\mathbf{j}) and FBTP aggregates and 2D SL films (\mathbf{k}), in which the peak between 1,450 cm⁻¹ and 1,370 cm⁻¹ can be assigned to the bending mode of the aliphatic CH₂ group (α (CH₂)) and the multipeaks in the range 1,620–1,540 cm⁻¹ could come from the C=C stretching of aromatic linkers.

at approximately 45° and 135°, which is consistent with the DFT energy calculation for the backbone dihedral torsion of the ligands (Supplementary Fig. 9). The energy (Fig. 3f) and molecular planarity parameter (Fig. 3g) distributions show similar results, in which FBTT has a narrower distribution, suggesting that FBTT is more planar and has a more ordered packing than FBTP (see the span of deviation from plane in Supplementary Fig. 10 for more information). These match our observations in the MD simulation in Fig. 3c,d. To examine the packing behaviour of each ligand, we conducted a free-energy analysis with respect to ligand rotation in the lattice (Fig. 3h). The reaction coordinate of the free energy is defined as the packing angle between the ligand being rotated and the reference ligand (Extended Data Fig. 6). It clearly shows that FBTT requires more energy than FBTP to break from parallel stacking (angle = 0°). Furthermore, the FBTP case has a plateau around 50-70°, indicating that FBTP ligands are prone to reorganize themselves to a non-parallel packing pattern in the lattice (Fig. 3h). All of the above analyses imply that FBTT is more planar and tends to have stronger intermolecular interactions, whereas FBTP is less planar and tends to behave like a single molecule in the lattice. These molecular-scale differences reveal the subtle aspects of ligand design that conduce the formation of SMAs on designated lattice incorporation.

To experimentally examine the molecular configuration and packing behaviours of organic emitters in the inorganic lattices, we resolved their single-crystal structures (Supplementary Table 1). Supplementary Figs. 11 and 12 show the single-crystal structures of FBTT-contained and FBTP-contained hybrid materials; respectively. The FBTT molecules in the perovskite lattice adopt a herringbone packing (Extended Data Fig. 7), which is a common motif for organic semiconductors. The torsion angle between the benzothiadiazole and thienyl rings is roughly 2° (Fig. 3i, left). By strong contrast, the packing motif of organic FBTP molecules in the perovskite lattice is dominated by two different stacking styles, criss-cross and herringbone (Extended Data Fig. 7). This unique stacking style of organic FBTP molecules is

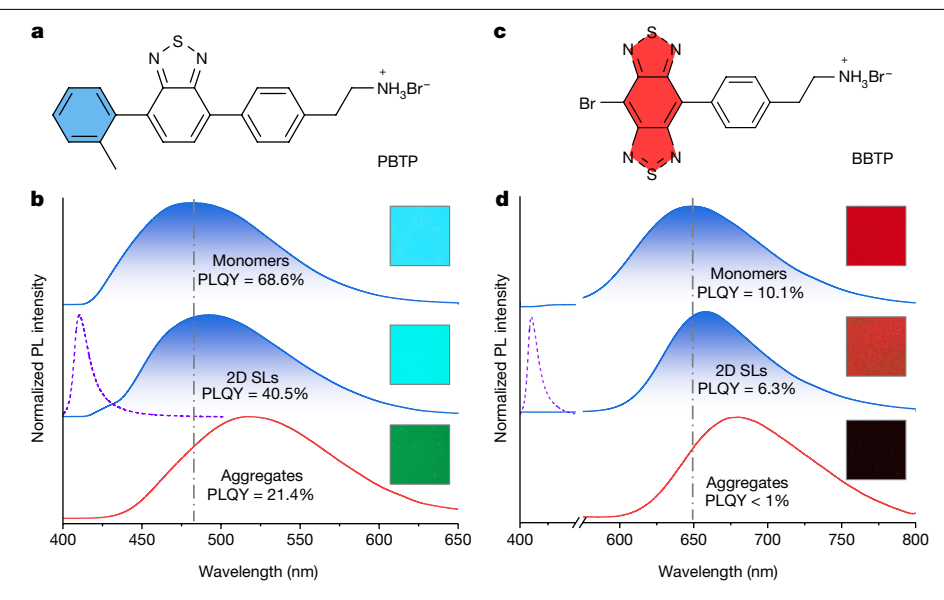


Fig. 4 | Single-molecule behaviour of other newly developed organic emitters in 2D SLs. a, Molecular structure of PBTP. b, PL spectra and PLQY of PBTP monomer in PMMA film, PBTP 2D SLs and PBTP aggregate films. c, Molecular structure of BBTP. d, PL spectra and PLQY of BBTP monomer in PMMA film, BBTP 2D SLs and BBTP aggregate films. The insets in **b** and **d** are PL images

of the corresponding thin-film samples and all the image scales are 10 μ m \times 10 μ m; the dashed violet curves are the PL spectra of (PEA)₂PbBr₄, which implies the emission feature of the 2D lead bromide lattice; and the grey dash-dot lines $indicate \, the \, PL \, peaks \, of \, the \, monomers \, compared \, with \, those \, of \, the \, 2D \, SLs \, and \,$ aggregates.

radically different from the normally observed herringbone or lamellar 2D π - π stacking (Supplementary Fig. 13) in organic-semiconductor crystals⁴⁰ and organic-molecule-incorporated 2D perovskite structures^{22,27,41}. Furthermore, the torsional angle between the benzothiadiazole and phenyl rings is found to be approximately 45° (Fig. 3i, right). All of the experimental outputs from single-crystal XRD results demonstrate that FBTT is more planar and has a more ordered packing than FBTP, which is in excellent agreement with our MD simulation predictions.

We performed Fourier-transform infrared (FTIR) spectroscopy to inspect the footprint of molecular structures and intermolecular interactions. Infrared absorption from 3,100 to 2,900 cm⁻¹ was typically assigned to the C-H stretching mode⁴² (Fig. 3j,k). In the FBTT case, the 2D SLs show a broad feature in this stretching region (Fig. 3i, red curve), which is identical to that of its aggregates (Fig. 3j, blue curve). Notably, we observed clear fine structures from FBTP SLs in this stretching region (Fig. 3k, red curve), which are absent in the corresponding aggregates (Fig. 3k, blue curve). The sharp peak at 2,960 cm⁻¹ corresponds to the asymmetrical stretching of CH₃ groups that are attached to the fluorene unit and the peaks around 3,050 cm⁻¹ (Fig. 3k) seem to come from the C-H stretch of the aromatic ring in FBTP molecules. These sharp peaks and fine structures indicate that FBTP molecules possess sufficient freedom to vibrate like single molecules in the perovskite lattice.

Chemical tunability of SMAs

We further developed two new single-molecule-like emitters with different emission colours. Specifically, replacing the fluorene unit with a weaker donor (tolyl group) generates a sky-blue emitter, PBTP (Fig. 4a; 2-(4-(7-(o-tolyl)benzo[c][1,2,5]thiadiazol-4-yl)phenyl) ethan-1-ammonium bromide). Also, substituting the benzothiadiazole group with a stronger acceptor (benzo[1,2-c:4,5-c']bis([1,2,5]thiadiazole)) produces a red emitter, BBTP (Fig. 4c; 8-bromobenzo[1,2-c:4,5-c'] bis([1,2,5]thiadiazole-4-yl)phenyl)ethan-1-ammonium bromide). TDDFT calculations confirmed reversed type I band alignment relative to [PbBr₄]²⁻lattice (Extended Data Fig. 1). In parallel, XRD, GIWAXS and UV-vis measurements (Extended Data Fig. 8) indicate that organic emitters were successfully incorporated into the lead bromide matrix. The PLOYs of 2D SLs are also much higher than that of the corresponding aggregates (Fig. 4b,d). Both PL emission wavelengths and PLQYs of 2D SLs are similar to that of the corresponding monomers and blueshifted from the aggregates, demonstrating the generality of our strategy. It is noteworthy that our observation is conceptually different from aggregation-induced emission⁴³, as aggregation-induced emission relies on the restriction of the intramolecular rotation of individual molecules, whereas our perovskite SLs maintain the single-molecular signature by regulating intermolecular distance at near-equilibrium state. Also, the newly developed 2D SLs exhibit greatly improved photostability when compared with the well-known (PEA)₂PbBr₄ (Supplementary Fig. 14).

Molecular-ensemble properties

Owing to the ordered molecular arrangement in the SLs, we investigated the angle-dependent PL emissions of FBTP-based films (Fig. 5a and Supplementary Fig. 15). The angular PL of monomer and aggregate films exhibit a typical emission profile of isotropic emitters (Fig. 5b and Supplementary Fig. 16). Notably, the FBTP SL demonstrates a strong anisotropic feature, in which the directional emissions centre around 50° (Fig. 5c). This specific angle is indeed perpendicular to the transition dipole of the organic emitters in the perovskite SLs (Supplementary Figs. 12 and 17). Moreover, we unambiguously observed a short-lived PL component in the FBTP SLs film, which is absent in FBTP monomers film that shows constant longer decay (Supplementary Fig. 18). To precisely resolve the timescale of the short-lifetime component, we conducted temperature-dependent streak-camera characterizations. Similarly, the FBTP monomers show consistent slow PL decay at different temperatures (Fig. 5d, f and Extended Data Fig. 9a,b); whereas a short-lived component (below 100 ps) in FBTP SLs is clearly presented across wide temperature regions (Fig. 5e,f, Extended Data Fig. 9c,d and Supplementary Table 2). Notably, such an ultrafast decay has not been reported in a conventional organic single-molecule system, which might be ascribed to the mutual interaction of the radiation field of those well-aligned neighbouring single molecules⁴⁴, linking to the behaviours of ordered molecular ensembles or aggregates⁴⁵⁻⁴⁹.

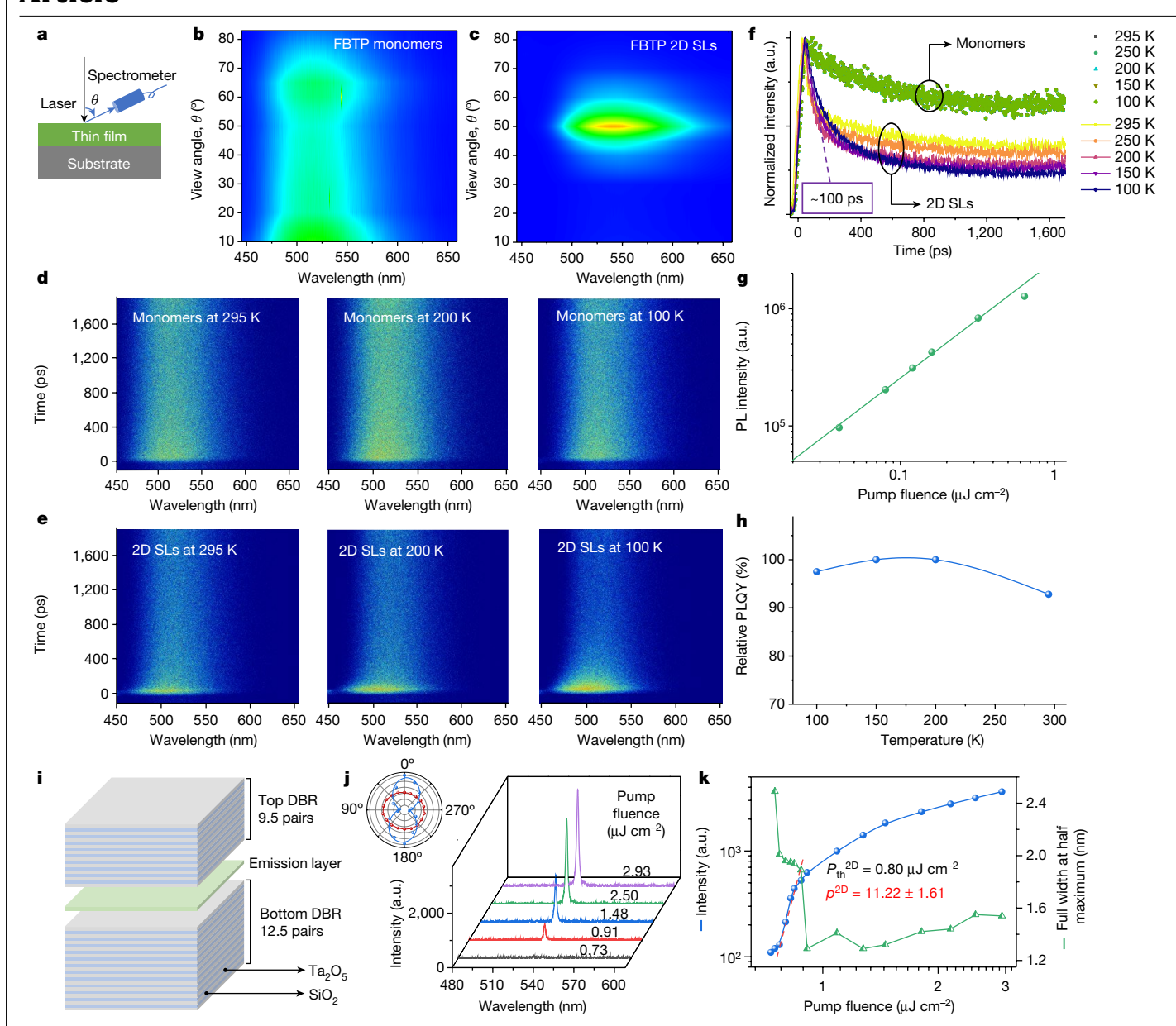


Fig. 5 | **SMA behaviour of organic emitters in 2D SLs. a**, Schematic of the angle-dependent PL measurement setup configuration. **b, c**, Angle-resolved PL of FBTP monomers (**b**) and 2D SLs (**c**). Note that an *s*-polarized laser was used as the excitation source. **d, e**, Streak-camera measurement results on FBTP monomers (**d**) and 2D SLs (**e**) at different temperatures. **f**, Extracted PL decay from steak-camera data shown in **d** and **e**. The decay curves for the monomers all overlapped at different temperatures. **g**, Power-dependent PL intensity of FBTP 2D SLs at room temperature. **h**, Relative PLQY of FBTP SLs at different temperatures, using room-temperature PLQY as a reference. **i**, Schematic

structure of lasing device with emission layer (that is, FBTP 2D SLs, monomers and aggregates) sandwiched between two DBRs. \mathbf{j} , PL spectra evolution of FBTP 2D SL under different pump fluences. Inset, polar plots of emission intensity at pump fluences below (red) and above (blue) the threshold. \mathbf{k} , Corresponding PL intensity against increasing pump fluences in log–log scale, showing a clear 'kink' at a threshold energy density of $P_{th}^{th} = 0.80~\mu\mathrm{J}~\mathrm{cm}^{-2}$. The intensity dependence is fitted to a power law x^p with $p^{2D} = 11.22$ above the threshold. a.u., arbitrary units.

Note that all of the temperature-dependent streak-camera results were measured with a fluence of 0.1 μ J cm⁻², which is below the exciton-exciton annihilation regime (Fig. 5g), thus excluding the possibility of bimolecular-process-induced fast decay. Moreover, the relative PLQYs of 2D SLs at different temperatures are all greater than 90% and reach unity (100%) at around 150–200 K (Fig. 5h and Supplementary Fig. 19). This implies that the non-radiative channels play an unimportant role in this ultrafast decay. One may notice the slight PLQY drop from 150 to 100 K, which can be ascribed to the inorganic sublattice contraction-induced emission quenching ^{50,51}. This observation also indirectly supports our hypothesis that the emitters are sustained as single molecules by the room-temperature perovskite lattice. Last, the PL spectra of short-lived

components of FBTP 2D SLs were slightly blueshifted compared with the longer components (Fig. 5e). On the basis of the intramolecular charge transfer nature of FBTP molecules (Supplementary Figs. 20 and 21), we believe that the short-wavelength emissions are probably coming from the locally excited states, which would be more feasible to undergo cooperatively radiative recombination.

We further conducted lasing characterizations by placing the emission layer between two high-reflectivity distributed Bragg reflectors (DBRs; Fig. 5i). As the pump power increases, the emission intensity from the FBTP 2D SL device steadily rises (Fig. 5j). When plotting the PL intensities against the pump fluences, a distinct 'kink' emerges at a threshold $P_{\rm th}^{\rm 2D}=0.80~\mu{\rm J}~{\rm cm}^{-2}$, which is accompanied by a sharp decline

in emission linewidth (Fig. 5k), linearly polarized output (inset in Fig. 5i and Supplementary Fig. 22) and outstanding coherence (Supplementary Fig. 23), demonstrating the transition from spontaneous emission to full lasing action. Furthermore, the superlinear intensity dependence is fitted to a power law $y = x^p$ with $p^{2D} = 11.22$ above the threshold for the 2D SL, which greatly exceeds that of the FBTP monomer ($p^{mon} = 1.70$ with $P_{\rm th}^{\rm mon}$ = 2.71 μ J cm⁻²; Extended Data Fig. 10a-e). Notably, lasing emission was not observed from the FBTP aggregates-based device, probably attributable to disorder and the ACQ effect (Extended Data Fig. 10f,g). These findings together validate that the exceptional gain performance of FBTP 2D SLs resulted from the organized molecular arrangement at a near-equilibrium intermolecular distance (Supplementary Table 3).

Discussion

We have successfully incorporated a wide range of organic emitters into the 2D perovskite lattice with tunable emissions spanning from blue to green and red. We found that the molecular emitters with a suitable intramolecular twist in the perovskite SLs could retain the characteristics of single molecules. Surprisingly, these molecular emitters in perovskite SLs also exhibit dense packing and strong alignment resembling aggregates, which leads to unusual emission behaviours such as directional emission, enhanced radiative recombination rates and low-threshold lasing. With a vast selection of organic emitters of desirable properties, the hybrid SL defines a rich family of optoelectronic materials for solid-state lighting applications. For instance, preliminary investigations on light-emitting diode devices demonstrate more than 50-fold enhancements in external quantum efficiency when the FBTP molecules are confined in the perovskite 2D SLs compared with their true aggregates (Supplementary Fig. 24). Finally, this approach could be applicable to other inorganic motifs (Supplementary Fig. 25), such as layered metal halide-organic heterostructures⁵², molecule-intercalated layered 2D atomic crystal SLs⁵³ and 1D or 0D organic-inorganic hybrid clusters 54,55, which are yet to be further explored. In brief, the SMA confined in perovskite 2D SLs go beyond the present classification of organic matter, such as typical H, Jor null aggregates^{56,57}, representing a previously undiscovered phase at a near-equilibrium distance.

Online content

Any methods, additional references, Nature Portfolio reporting summaries, source data, extended data, supplementary information, acknowledgements, peer review information; details of author contributions and competing interests; and statements of data and code availability are available at https://doi.org/10.1038/s41586-024-07925-9.

- Tang, C. W. & VanSlyke, S. A. Organic electroluminescent diodes. Appl. Phys. Lett. 51, 1. 913-915 (1987).
- Uoyama, H., Goushi, K., Shizu, K., Nomura, H. & Adachi, C. Highly efficient organic light-2. emitting diodes from delayed fluorescence. Nature 492, 234-238 (2012).
- Tessler, N., Denton, G. J. & Friend, R. H. Lasing from conjugated-polymer microcavities. Nature 382, 695-697 (1996). Kozlov, V. G., Bulović, V., Burrows, P. E. & Forrest, S. R. Laser action in organic semiconductor
- waveguide and double-heterostructure devices. Nature 389, 362-364 (1997)
- 5 Samuel, I. D. W. & Turnbull, G. A. Organic semiconductor lasers. Chem. Rev. 107, 1272-1295 (2007).
- 6. Toninelli, C. et al. Single organic molecules for photonic quantum technologies. Nat. Mater. 20, 1615-1628 (2021).
- Hail, C. U. et al. Nanoprinting organic molecules at the quantum level. Nat. Commun. 10, 1880 (2019).
- Carter, K. P., Young, A. M. & Palmer, A. E. Fluorescent sensors for measuring metal ions in living systems. Chem. Rev. 114, 4564-4601 (2014).
- Yang, Y., Zhao, Q., Feng, W. & Li, F. Luminescent chemodosimeters for bioimaging. Chem. Rev. 113, 192-270 (2013).
- Cosco, E. D. et al. Flavylium polymethine fluorophores for near- and shortwave infrared imaging. Angew. Chem. Int. Ed. 56, 13126-13129 (2017).
- Hong, Y., Lam, J. W. Y. & Tang, B. Z. Aggregation-induced emission: phenomenon, mechanism and applications. Chem. Commun. 29, 4332-4353 (2009)

- Lane, P. A. et al. Origin of electrophosphorescence from a doped polymer light emitting diode, Phys. Rev. B 63, 235206 (2001).
- Wang, H. et al. Doped organic crystals with high efficiency, color-tunable emission toward laser application. Cryst. Growth Des. 9, 4945-4950 (2009)
- Mischok, A., Hillebrandt, S., Kwon, S. & Gather, M. C. Highly efficient polaritonic lightemitting diodes with angle-independent narrowband emission. Nat. Photon. 17, 393-400
- Vietze, U. et al. Zeolite-dye microlasers. Phys. Rev. Lett. 81, 4628-4631 (1998).
- 16. Yu. J. et al. Confinement of pyridinium hemicyanine dve within an anionic metal-organic framework for two-photon-pumped lasing. Nat. Commun. 4, 2719 (2013).
- Fang, Q. et al. Designed synthesis of large-pore crystalline polyimide covalent organic frameworks, Nat. Commun. 5, 4503 (2014).
- 18. Huang, Y. et al. Reducing aggregation caused quenching effect through co-assembly of PAH chromophores and molecular barriers. Nat. Commun. 10, 169 (2019).
- Hua, B. et al. Supramolecular solid-state microlaser constructed from pillar[5]arene-based host-guest complex microcrystals. J. Am. Chem. Soc. 140, 15651-15654 (2018).
- 20. Kim, D.-H. et al. High-efficiency electroluminescence and amplified spontaneous emission from a thermally activated delayed fluorescent near-infrared emitter, Nat. Photon, 12. 98-104 (2018).
- Mitzi, D. B., Feild, C. A., Harrison, W. T. A. & Guloy, A. M. Conducting tin halides with a layered organic-based perovskite structure. Nature 369, 467-469 (1994).
- Gao, Y. et al. Molecular engineering of organic-inorganic hybrid peroyskites quantum wells, Nat. Chem. 11, 1151-1157 (2019).
- Smith, M. D., Connor, B. A. & Karunadasa, H. I. Tuning the luminescence of layered halide perovskites, Chem. Rev. 119, 3104-3139 (2019).
- Leng, K., Fu, W., Liu, Y., Chhowalla, M. & Loh, K. P. From bulk to molecularly thin hybrid perovskites. Nat. Rev. Mater. 5, 482-500 (2020).
- Li, X., Hoffman, J. M. & Kanatzidis, M. G. The 2D halide perovskite rulebook: how the spacer influences everything from the structure to optoelectronic device efficiency. Chem. Rev. 121, 2230-2291 (2021).
- Gong, X, et al. Electron-phonon interaction in efficient perovskite blue emitters. Nat. Mater. 17. 550-556 (2018).
- Passarelli, J. V. et al. Enhanced out-of-plane conductivity and photovoltaic performance in n = 1 layered perovskites through organic cation design. J. Am. Chem. Soc. 140, 7313-7323 (2018)
- Yan, L., Gloor, C. J., Moran, A. M. & You, W. Non-covalent interactions involving π effect between organic cations in low-dimensional organic/inorganic hybrid perovskites. Appl. Phys. Lett. 122, 240501 (2023).
- Wang, N. et al. Perovskite light-emitting diodes based on solution-processed self-organized multiple quantum wells. Nat. Photon. 10, 699-704 (2016)
- Wang, K. et al. Suppressing phase disproportionation in quasi-2D perovskite light-emitting diodes, Nat. Commun. 14, 397 (2023).
- Tsai, H. et al. High-efficiency two-dimensional Ruddlesden-Popper perovskite solar cells. Nature 536, 312-316 (2016).
- Feng, J. et al. Single-crystalline layered metal-halide perovskite nanowires for ultrasensitive photodetectors. Nat. Electron. 1, 404-410 (2018).
- Qin, C, et al. Stable room-temperature continuous-wave lasing in quasi-2D perovskite films. Nature 585, 53-57 (2020).
- Era, M., Maeda, K. & Tsutsui, T. Enhanced phosphorescence from naphthalene chromophore incorporated into lead bromide-based layered perovskite having organicinorganic superlattice structure, Chem. Phys. Lett. 296, 417-420 (1998).
- Chondroudis, K. & Mitzi, D. B. Electroluminescence from an organic-inorganic perovskite incorporating a quaterthiophene dye within lead halide perovskite layers. Chem. Mater 11. 3028-3030 (1999).
- Braun, M., Tuffentsammer, W., Wachtel, H. & Wolf, H. C. Pyrene as emitting chromophore in organic-inorganic lead halide-based layered perovskites with different halides. Chem. Phys. Lett. 307, 373-378 (1999).
- Ema, K., Inomata, M., Kato, Y., Kunugita, H. & Era, M. Nearly perfect triplet-triplet energy transfer from Wannier excitons to naphthalene in organic-inorganic hybrid quantum-well materials. Phys. Rev. Lett. 100, 257401 (2008).
- 38. Karl, M. et al. Flexible and ultra-lightweight polymer membrane lasers. Nat. Commun. 9. 1525 (2018).
- Silver S. Yin, I. Li, H. Brédas, I.-L. & Kahn, A. Characterization of the valence and conduction band levels of n = 12D perovskites: a combined experimental and theoretical investigation. Adv. Energy Mater. 8, 1703468 (2018).
- Gryn'ova, G., Lin, K.-H. & Corminboeuf, C. Read between the molecules: computational insights into organic semiconductors. J. Am. Chem. Soc. 140, 16370-16386 (2018).
- Mitzi, D. B., Chondroudis, K. & Kagan, C. R. Design, structure, and optical properties of organic-inorganic perovskites containing an oligothiophene chromophore. Inorg. Chem. 38, 6246-6256 (1999).
- Chung, C., Lee, M. & Choe, E. K. Characterization of cotton fabric scouring by FT-IR ATR spectroscopy. Carbohydr. Polym. 58, 417-420 (2004).
- 43. Hong, Y., Lam, J. W. Y. & Tang, B. Z. Aggregation-induced emission, Chem. Soc. Rev. 40. 5361-5388 (2011).
- 44. Gómez-Castaño, M. et al. Energy transfer and interference by collective electromagnetic coupling, Nano Lett. 19, 5790-5795 (2019).
- 45. Rainò, G. et al. Superfluorescence from lead halide perovskite quantum dot superlattices. Nature 563, 671-675 (2018).
- 46. Cherniukh, I. et al. Perovskite-type superlattices from lead halide perovskite nanocubes. Nature 593, 535-542 (2021).
- Spano, F. C., Kuklinski, J. R. & Mukamel, S. Temperature-dependent superradiant decay of excitons in small aggregates. Phys. Rev. Lett. 65, 211-214 (1990).
- Blach, D. D. et al. Superradiance and exciton delocalization in perovskite quantum dot superlattices, Nano Lett. 22, 7811-7818 (2022).
- Findik, G. et al. High-temperature superfluorescence in methyl ammonium lead iodide. Nat. Photon. 15, 676-680 (2021).

- Dursun, I. et al. Temperature-dependent optical and structural properties of chiral twodimensional hybrid lead-iodide perovskites. J. Phys. Chem. C 127, 15423–15434 (2023).
- Chen, H. et al. Structural and spectral dynamics of single-crystalline Ruddlesden-Popper phase halide perovskite blue light-emitting diodes. Sci. Adv. 6, eaay4045 (2020).
- Aubrey, M. L. et al. Directed assembly of layered perovskite heterostructures as single crystals. Nature 597, 355-359 (2021).
- Qian, Q. et al. Chiral molecular intercalation superlattices. Nature 606, 902-908 (2022).
- 54. Yuan, Z. et al. One-dimensional organic lead halide perovskites with efficient bluish white-light emission. Nat. Commun. 8, 14051 (2017).
- 55. Zhou, C. et al. Blue emitting single crystalline assembly of metal halide clusters. J. Am. Chem. Soc. 140, 13181-13184 (2018).
- 56. Hestand, N. J. & Spano, F. C. Molecular aggregate photophysics beyond the Kasha model: novel design principles for organic materials. Acc. Chem. Res. 50, 341-350 (2017).
- Kaufmann, C., Bialas, D., Stolte, M. & Würthner, F. Discrete π-stacks of perylene bisimide $\ \, \text{dyes within folda-dimers: insight into long- and short-range exciton coupling.} \textit{ J. Am. }$ Chem. Soc. 140, 9986-9995 (2018).

Publisher's note Springer Nature remains neutral with regard to jurisdictional claims in published maps and institutional affiliations.

Springer Nature or its licensor (e.g. a society or other partner) holds exclusive rights to this article under a publishing agreement with the author(s) or other rightsholder(s); author self-archiving of the accepted manuscript version of this article is solely governed by the terms of such publishing agreement and applicable law.

© The Author(s), under exclusive licence to Springer Nature Limited 2024

Methods

Chemicals and reagents

Organic solvents including anhydrous N,N-dimethylformamide (DMF), chlorobenzene (CB) and dichloromethane (DCM), acetonitrile (ACN), o-dichlorobenzene (DCB) and solid chemicals including lead bromide (PbBr $_2$) were purchased from Sigma-Aldrich. All of the above chemicals were used as received. All chemical reagents and solvents for organic molecular emitter synthesis were purchased from Combi-Blocks and used as received. More details on the synthesis of organic molecular emitters, FBTT, FBTP, PBTP and BBTP, can be found in the Supplementary Information.

Thin-film fabrication

(1) The precursor solution for perovskites (2D SLs) was formulated with a concentration of 50 mM by dissolving organic emitters (that is, FBTT, FBTP, PBTP, BBTP, PEA) and PbBr₂ in DMF with a stoichiometry ratio of 2:1 inside the nitrogen-filled glovebox. (2) The precursor solution for monomers was prepared by mixing 1 mg of organic emitters and 50 mg of PMMA with 1 ml mixed solvent (CB:DMF $_{v/v}$ = 1:1) and then stirring continuously at 100 °C overnight to obtain homogeneous polymer solutions. The weight percentage of organic emitters relative to PMMA is set at 2 wt% to ensure that organic emitters can be considered as isolated single molecules without experiencing obvious ACQ effect. (3) The precursor solution for aggregates was made by dissolving 10 mg of organic emitters in 1 ml DMF. All of the solutions were then saved for further use. Bare Si/SiO₂ wafer, quartz, glass slides or DBRs were cleaned by ultrasonication in detergent, deionized water, acetone and isopropanol for 15 min each and then dried with dry air. (4) The substrates were treated with UV-ozone for 20 min and then transferred into a glovebox for spin coating. The above precursor solutions were spin-coated onto the pre-cleaned substrates at 2,000 rpm for 60 s, followed by thermal annealing on a hot plate at 150 °C for 10 min. These obtained films were used for further characterizations.

Bulk single-crystal growth

The FBTP-contained 2D SL single crystal was obtained through a vapour-diffusion method. Specifically, a 2:1 molar ratio of FBTP and PbBr₂ was dissolved in DMF to make a 25-mM solution by heating at 70 °C for 1 h. Then, 0.1 ml of precursor solution was injected into a 4-ml small vial and placed in a 20-ml large vial containing 3 ml of a mixed solvent of CB and DCM with a volume ratio of 2:1, which was immediately sealed with a cap. The system was left undisturbed in a refrigerator (about 4 °C) for one month, yielding thin green plates. The FBTT-contained 2D SL single crystals were obtained through slow-cooling crystallization using a solution composed of approximately 1 mg of FBTT, 20 mg of lead bromide (PbBr₂), 200 μl of hydrobromide acid (HBr, 48 wt% in H₂O) and 300 µl of ethanol. Ethanol was added to assist the dissolution of the organic cations and crystallization. After mixing the precursors and solution, the contents of the sample vial were heated to over 100 °C by a heat gun until all of the materials were completely dissolved and the solution was clear. The vials were then moved to a Dewar flask water bath at 95 °C to cool down for 72 huntil it reached room temperature. With this process, yellowish-orange bulk single crystals were obtained in the form of thin plates.

Single-crystalline nanocrystal growth

2D perovskite nanocrystals were synthesized using a modified co-solvent evaporation method 58 . 0.02 mmol of LBr (L = PEA, FBTT, FBTP) and 0.01 mmol of PbBr₂ precursors were dissolved in a 2-ml solution of DMF and CB mixed in a 1:1 volume ratio to prepare 5-mM stock solutions. The concentrated PEA precursor solution was then diluted 120 times using a co-solvent system of CB, AN and DCB mixed in a volume ratio of 2.5:1:0.01. For (FBTT)₂PbBr₄ and (FBTP)₂PbBr₄, the stock

solution was diluted 720 times by CB/AN/DCB co-solvent with a volume ratio of 7.4:1:0.01. A Si/SiO $_2$ substrate was placed inside a 20-ml glass vial kept on a hot plate at 70 °C. Approximately 10 μ l of the diluted precursor was then dropped on the Si/SiO $_2$ substrate. The solvent evaporation is associated with the nucleation and growth of the nanocrystals on the substrate. The substrate was then removed from the hot plate in about 10 min, once all the solvent was evaporated.

DBR device fabrication

Three DBR devices were fabricated by sandwiching thin-film layers of FBTP 2D SLs, FBTP aggregates and FBTP monomers, respectively, between two highly reflective DBRs. The bottom DBR was first fabricated by an e-beam evaporator, consisting of 12.5 pairs of silicon dioxide (92.4 nm) and tantalum pentoxide (61.8 nm) capped by silicon dioxide. The emission layer was then spin-coated on the bottom DBR, for which the thickness was adjusted to approximately 140 nm by controlling the spin speed or the concentration of precursor solutions. Finally, the bottom DBR with the emission layer on top was transferred into the e-beam evaporator chamber again to complete the fabrication of a top DBR, which consists of nine pairs of silicon dioxide (91.8 nm) and tantalum pentoxide (65.6 nm).

Characterizations

NMR spectra. Nuclear magnetic resonance (NMR) spectra were acquired at room temperature using a Bruker AV 400-MHz spectrometer with CDCl₃ or DMSO- d_6 as the solvent and tetramethylsilane (TMS) as an internal standard. Chemical shifts of ¹H NMR and ¹³C NMR signals were reported as values (ppm) relative to the TMS standard.

Mass spectra. High-resolution mass spectrometry was acquired in positive electrospray mode on an LTQ Orbitrap XL instrument (Thermo Fisher Scientific).

Single-crystal XRD analysis. Single crystals were analysed using a Bruker Quest diffractometer with kappa geometry, an I- μ -S microsource X-ray tube, a laterally graded multilayer Göbel mirror for single-crystal monochromatization and an area detector (Photon2 CMOS). Data collections were conducted at 150 K with Cu K α radiation (λ = 1.54178 Å).

UV-vis absorption spectra. Thin-film absorption spectra were recorded on an Agilent UV-Vis-NIR Cary 5000 spectrometer in transmission mode.

PL spectra. Steady-state PL spectra were obtained with an Olympus microscope system (BX53) integrated with an X-CITE 120Q UV lamp. The filter cube contains a band-pass filter (330–385 nm) for excitation, a dichroic mirror (cut-off wavelength 400 nm) for light splitting and a 420-nm long-pass filter for emission collection. The collected PL signals were analysed by a spectrometer (SpectraPro HRS-300).

PLQY. The thin-film samples for PLQY measurements were deposited onto quartz substrates by following the preparation of precursor solutions and the fabrication procedures detailed in the 'Thin-film fabrication' subsection. The absolute PLQYs at room temperature were obtained by a three-step technique with a home-designed system, which consists of a continuous-wave laser (375 nm), an integrating sphere, optical fibre and a spectrometer. The relative PLQYs at low temperatures were estimated on the basis of the integrated emission intensity of the PL spectra at different temperatures for the 2D SLs film. By taking the PLQY of the sample at room temperature as a reference and correcting for absorption⁴⁸, the relative PLQYs of the film were then calculated.

Powder XRD. Thin-film XRD was collected with Rigaku SmartLab (Cu K α , λ = 1.54056 Å) in Bragg–Brentano mode.

Thickness measurement. The thickness of the thin-film samples was measured with a Bruker DektakXT stylus profilometer. Here the thickness of FBTT, FBTP, PBTP, BBTP and PEA 2D SLs samples were determined to be 55.3, 58.2, 24.3, 23.1 and 20.8 nm, respectively.

Atomic force microscopy. The surface morphology and roughness were obtained with a MultiMode 8-HR AFM (Bruker) in tapping mode.

Scanning electron microscopy. Thin-film scanning electron microscopy images were acquired with a high-resolution field-emission scanning electron microscope (SU8010).

FLIM. FLIM measurements were performed using a Nikon TE2000 confocal microscope with water immersion objective ($60 \times$, NA = 1.2) equipped with an Alba Fast FLIM system (ISS). Specifically, samples were excited using a 440-nm pulsed laser with modulation frequency of 10 MHz and imaged through a 506-nm long-pass filter, followed by MPD APD detectors. After image collection, biexponential fitting of FLIM images was performed using VistaVision software (ISS) to obtain the fluorescent lifetimes of each pixel.

GIWAXS. GIWAXS spectra were collected at beamline 7.3.3 at the Advanced Light Source at Lawrence Berkeley National Laboratory using an incident angle of 0.18° and wavelength of 1.24 Å (energy 10 keV). The detector used was PILATUS 2M (Dectris, Inc.) and the data were calibrated using silver behenate as a standard using the Nika Igor Pro package⁵⁹.

FTIR. Attenuated total reflectance FTIR spectroscopy was conducted on a Thermo Nicolet Nexus 470 FTIR, equipped with a diamond-attenuated total reflectance crystal sampling accessory, with N_2 purging.

Low-temperature PL and time-resolved PL measurements. A homebuilt confocal micro-PL setup was used to carry out temperaturedependent steady-state and time-resolved optical measurements. A 447-nm picosecond pulsed diode laser (LDH-P-C-450B, PicoQuant, 50 ps, 5 MHz) was used as the excitation source and focused onto the surface of the samples using a Nikon objective ($40 \times$, NA = 0.6). The emitted signal was collected by the same objective, dispersed with a monochromator (Andor Technology) and detected by a spectrometer (Andor Shamrock 3030i) and charge-coupled device (CCD: Andor Newton 920). The excitation scatter was rejected using a suitable optical filter placed before the detector. For the time-resolved PL dynamics, the signal was detected by a single-photon avalanche diode (PicoQuant, PDM Series) with a single-photon counting module (PicoQuant), with a time resolution of about 100 ps. For most of the measurements, a low excitation fluence of 0.1 μJ cm⁻² was used to prevent the onset of parasitic bimolecular processes such exciton–exciton annihilation.

For the temperature-dependent PL measurements, a closed-cycle optical cryostat Cryostation s50 (Montana Instruments) was used. The sample was placed on the holder and a hard vacuum was established in the sample chamber. Temperatures in the range 100–295 K, with a temperature stability <10 mK, were then attainable using the control units.

Angle-dependent PL measurements. Angle-resolved PL measurements were performed on a home-built system. The sample is illuminated with a pulsed laser (100 fs, 400 nm) produced by the second-harmonic generation from a Ti:sapphire laser system. The laser pulse polarization is controlled by a polarizer and half-wave plate and impinges on the sample at normal incidence. The excited PL light is collected by a lens coupled to an optical fibre and finally directed into a spectrometer. The angle subtended by the lens is approximately 1°.

Temperature-dependent streak-camera measurements. The samples were excited with 440-nm-wavelength light pulses from an

ORPHEUS optical parametric amplifier powered by a Pharos amplifier with a 2-kHz repetition rate and 170-fs pulse duration. The beam was focused with a lens into a 1-mm spot size on the sample that was mounted in a cryostat and held under a vacuum of $<\!8\times10^{-5}$ mbar. The PL was collected by an achromatic lens and guided into a spectrograph (Andor Kymera 328i), which was connected to a charge-coupled device camera (Andor iXon Life 888) and streak camera (Hamamatsu C10910) for performing time-integrated PL and time-resolved PL measurements, respectively.

Photostability test. The photostability test on the 2D perovskite thin-film samples were carried out by tracking their absorption spectra under the irradiation of a UV curing lamp in a glovebox, in which the UV lamp had an output power of 0.31 W cm⁻² and was 5 cm away from the samples.

Lasing characterizations. Optically pumped lasing measurements were carried out on a home-built far-field micro-PL system in ambient conditions. The excitation pulses (400 nm, about 100 fs, 1 kHz) were generated from the second harmonic of the fundamental output of a regenerative amplifier (Solstice, Spectra-Physics, 800 nm, about 100 fs, 1 kHz), which was in turn seeded by a mode-locked Ti:sapphire laser (Mai Tai, Spectra-Physics, 800 nm, about 100 fs, 80 MHz). The DBR devices with emission layer sandwiched between two DBRs were locally excited with a laser beam focused down to about 50 μ m in diameter through an objective (Nikon CFLU Plan, 5×, NA = 0.15), with input power altered by neutral density filters. After passing through a 420-nm long-pass emission filter, the collected PL signal from the DBR devices was subsequently coupled to a grating spectrometer (Acton SP-2358) and recorded with a thermoelectrically cooled CCD (Princeton Instruments, ProEm 1600B).

Coherence measurements. The spatial coherence of the lasing emission from the DBR device was evaluated by a Michelson interferometer setup. Initially, the emission from the DBR device was divided into two beams with a beam splitter, which were subsequently directed to two separate arms of the interferometer. These beams were then reflected by the interferometer mirrors and overlapped on a CCD camera. The length of one interferometer arm was precisely adjusted to ensure that both beams travelled the same distance before reaching the CCD camera. Clear interference fringes will be recorded if the initial emission exhibits coherence.

Simulations

MD simulations. Unbiased MD sampling: the modified MYP model was used for all simulations, as described in our previous work. LAMMPS and PLUMED were used to perform the MD simulations. All simulations used a 1-fs integration time step and periodic boundary conditions. Long-range electrostatics was modelled using the particle-particleparticle-mesh (PPPM) algorithm and Lennard-Jones interactions were truncated at 15 Å. The initial structure of 2D perovskites was generated by constructing representative unit cells of ideal perovskites lattice with the bulky organic cations placed at the surface. The simulation was first relaxed in the NVE ensemble with restrained atomic displacements of 0.01 Å per time step for 50 ps, followed by a 100-ps NPT equilibration with the Nosé-Hoover thermostat and barostat. The boundary of the y direction, which is parallel to the bulky organic cations, is extended by 20 Å to prevent the interaction of organic cations from different sides as a result of periodic boundary conditions. During the NPT equilibration, the barostat was only applied to the x and z directions, which are normal to the bulky organic cations. Finally, a 100-ps NVT simulation is conducted to evaluate the distribution of backbone dihedrals, the site energy of ligands and the molecular planarity parameter.

Free-energy calculation on the ligand rotation: the reaction coordinate of the free-energy calculation is defined as the angle between the

fitted planes of two randomly picked neighbouring ligands. Steered MD was then used to calculate the free-energy curve. In steered MD, we use a spring constant of 1,000 kcal (mol-Å) $^{-1}$ and a constant velocity of 0.0125 rad ps $^{-1}$ to steer the ligand into the target-packing angle. All of the reported results are calculated on the basis of five independent simulation runs.

DFT calculations. Geometry optimizations and excited-state calculations for FBTT, FBTP, PBTP and BBTP molecules were carried out by means of DFT and TDDFT as implemented in the Gaussian 16 package⁶⁰ using the B3LYP functional⁶¹ and the def2-TZVP basis set⁶² in vacuum. The alkylammonium tail is not included for brevity, which tends to be flexible and varies its geometry depending on the matrix. In our experience, an expensive basis set such as def2-TZVP is necessary to achieve adequate accuracy in TDDFT calculations when considering the band alignment in perovskites. Transition dipole moments were visualized with the Multiwfn software⁶³.

Optical-field-distribution simulation. The electric-field intensity distribution in the 2D SLs-based DBR device was calculated in the electromagnetic-wave-frequency domain by using the commercial software COMSOL Multiphysics. A periodic boundary condition was applied to the modelling configuration. The transmitted spectrum was retrieved by setting the bottom side of the 2D SLs layer as a periodic excitation port.

Reporting summary

Further information on research design is available in the Nature Portfolio Reporting Summary linked to this article.

Data availability

Crystallographic data for the structure of FBTT-contained and FBTP-contained 2D SLs reported in this article have been deposited at the Cambridge Crystallographic Data Centre under deposition numbers CCDC 2289715 and 2283333, respectively. Copies of the data can be obtained free of charge at https://www.ccdc.cam.ac.uk/structures/. All other data supporting the findings of this study are available in the article and its Supplementary Information. Source data are provided with this paper.

 Shi, E. et al. Two-dimensional halide perovskite lateral epitaxial heterostructures. *Nature* 580, 614–620 (2020).

- Ilavsky, J. Nika: software for two-dimensional data reduction. J. Appl. Crystallogr. 45, 324–328 (2012).
- 60. Gaussian 16, Revision C.01 (Gaussian, Inc., 2016).
- Stephens, P. J., Devlin, F. J., Chabalowski, C. F. & Frisch, M. J. Ab initio calculation of vibrational absorption and circular dichroism spectra using density functional force fields. J. Phys. Chem. 98, 11623–11627 (1994).
- Weigend, F. & Ahlrichs, R. Balanced basis sets of split valence, triple zeta valence and quadruple zeta valence quality for H to Rn: design and assessment of accuracy. *Phys. Chem. Chem. Phys.* 7, 3297–3305 (2005).
- Lu, T. & Chen, F. Multiwfn: a multifunctional wavefunction analyzer. J. Comput. Chem. 33, 580–592 (2012).
- Brunner, K., Tortschanoff, A., Warmuth, C., Bässler, H. & Kauffmann, H. F. Site torsional motion and dispersive excitation hopping transfer in π-conjugated polymers. J. Phys. Chem. B 104, 3781–3790 (2000).
- Meskers, S. C. J., Hübner, J., Oestreich, M. & Bässler, H. Dispersive relaxation dynamics of photoexcitations in a polyfluorene film involving energy transfer: experiment and Monte Carlo simulations. J. Phys. Chem. B 105, 9139–9149 (2001).

Acknowledgements This work is supported by the National Science Foundation (grant nos. 2131608-ECCS and 2143568-DMR). A.D. acknowledges the support for spectroscopy measurements from the US Department of Energy, Office of Science, Office of Basic Energy Sciences under award no. DE-SC0022082. Z.-Y.L. and B.M.S. acknowledge the support for MD simulations from the US Department of Energy, Office of Energy Efficiency and Renewable Energy (EERE) under the Solar Energy Technologies Office award DE-EE0009519. The views expressed herein do not necessarily represent the views of the US Department of Energy or the United States Government. Work at Yale was supported by the Air Force Office of Scientific Research under grant no. FA9550-22-1-0209. C.B.F., A.B. and V.M.S. acknowledge the support of the Office of Naval Research (ONR) under award no. N00014-21-1-2026 and the Air Force Office of Scientific Research under grant no. FA9550-22-1-0372. We thank J. Simon for establishing the angle-dependent PL setup, Q. Hu for the help with mass-spectrometry measurements, L. Huang and M. Gather for discussions, and H. Liu for spatial-coherence measurements.

Author contributions L.D. conceived the idea. L.D. and B.M.S. supervised the project. K.W. carried out the materials synthesis, structural characterizations, film fabrication and data analysis. Z.-Y.L. and B.M.S. performed MD simulations and data analysis. A.D. conducted the low-temperature PL and time-resolved PL measurements and data analysis. C.A.K. and P.G. carried out streak-camera measurements. W.S. helped with DFT calculations on band alignment. H.Y. carried out FLIM measurements and data analysis. Z.H. and Y.S.Z. helped with DBR device fabrication and lasing characterizations. A.H.C. and C.Z. performed GIWAXS measurements. Y.T. conducted FTIR spectroscopy measurements. A.B. and V.M.S. supervised the optical-characterization-related activities and C.B.F. conducted angle-resolved PL measurements. D.V. contributed to ligand design and synthesis. K.W. and L.D. wrote the manuscript. All authors discussed the results and revised the manuscript.

Competing interests The authors declare no competing interests.

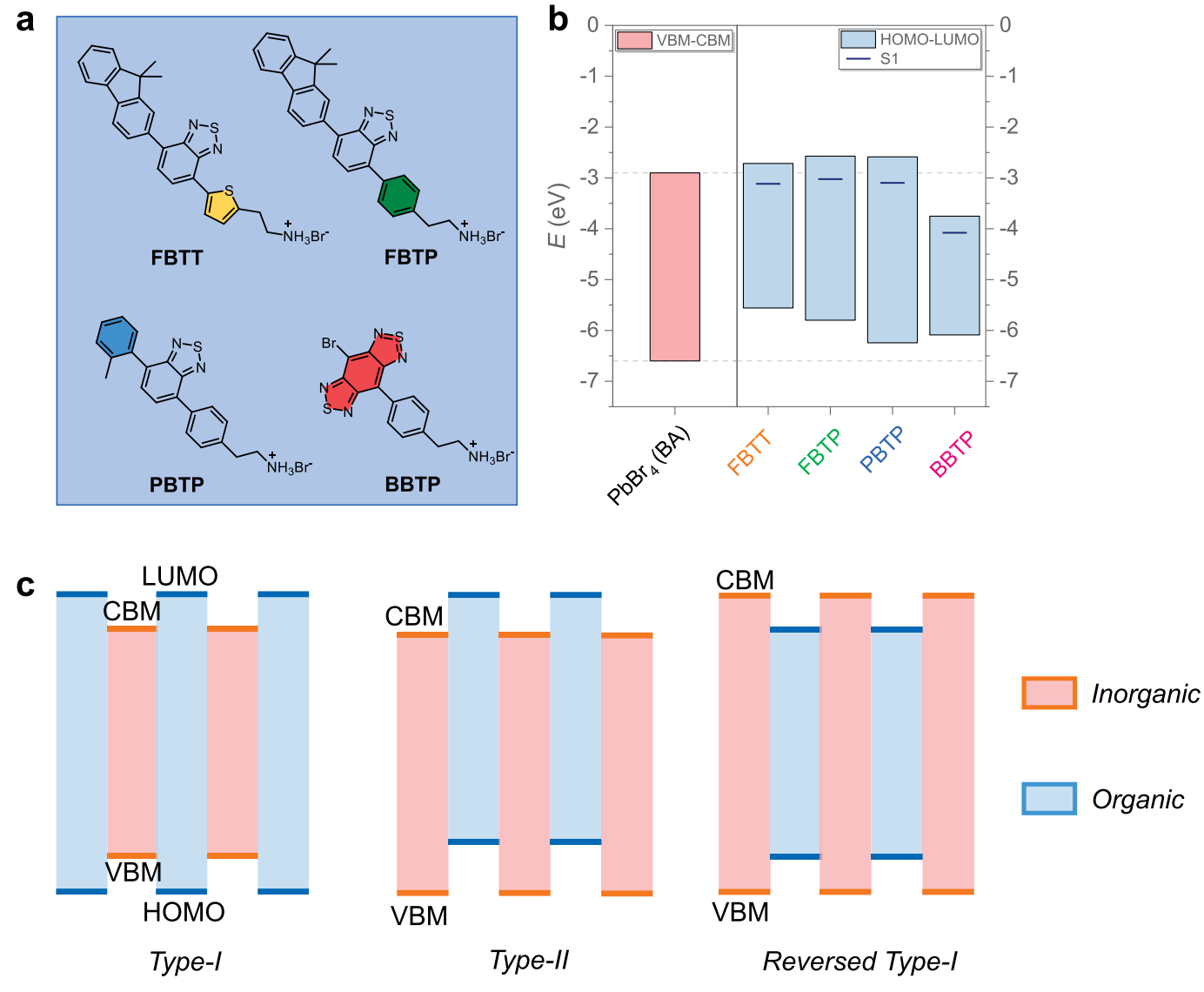
Additional information

Supplementary information The online version contains supplementary material available at https://doi.org/10.1038/s41586-024-07925-9.

Correspondence and requests for materials should be addressed to Brett M. Savoie or Letian Dou.

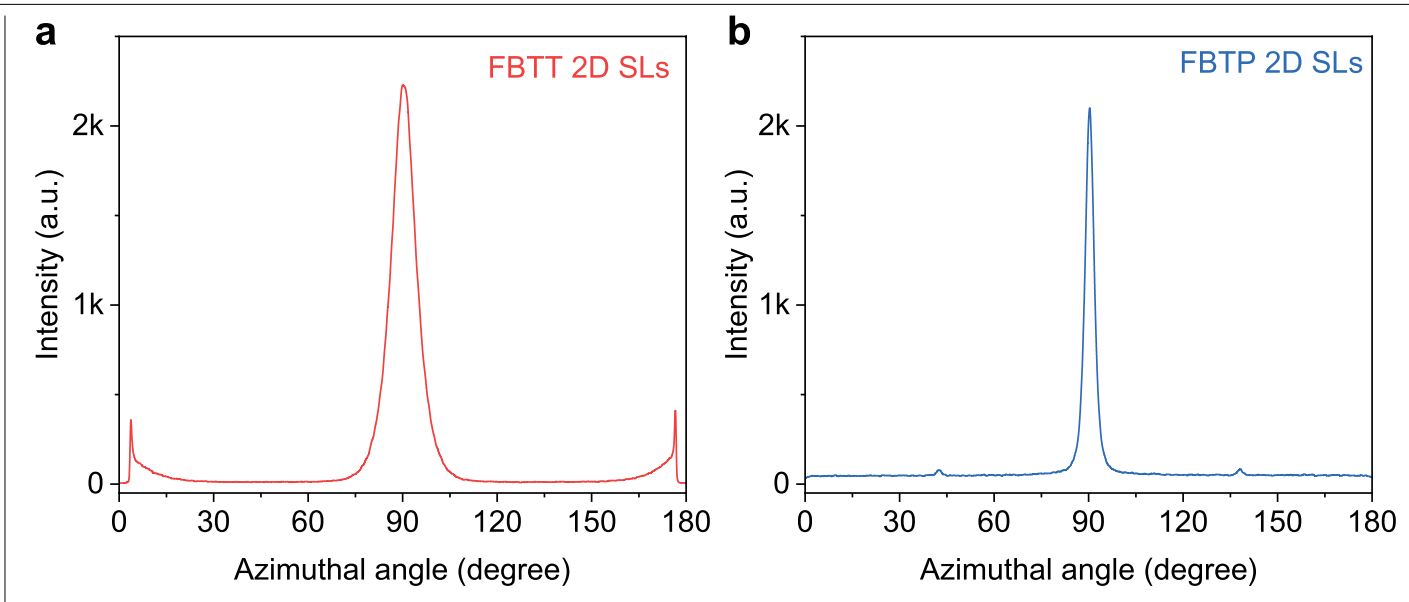
Peer review information *Nature* thanks the anonymous reviewers for their contribution to the peer review of this work. Peer reviewer reports are available.

Reprints and permissions information is available at http://www.nature.com/reprints.



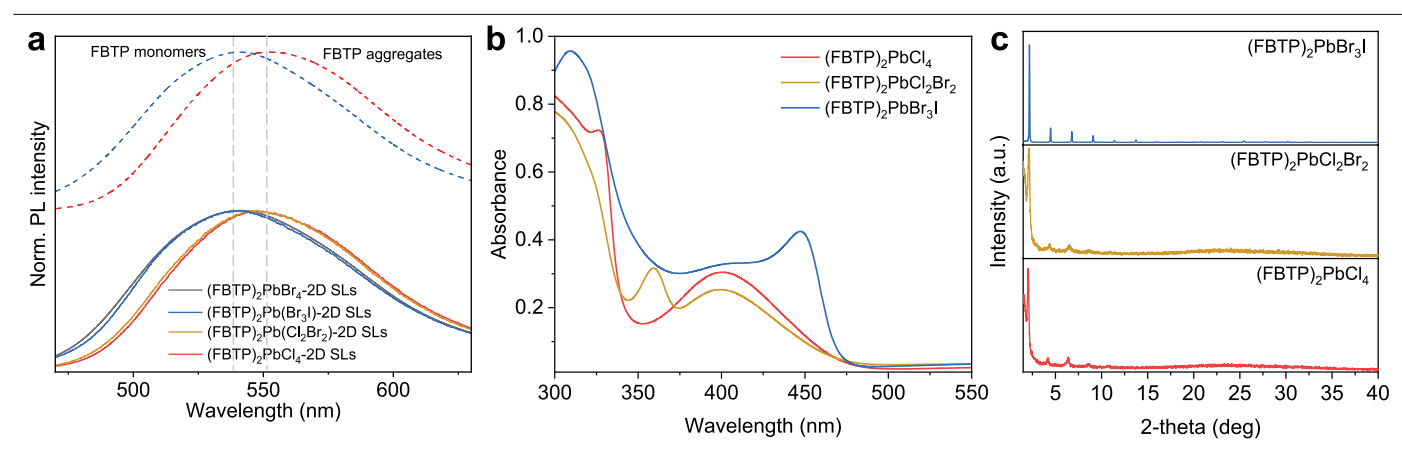
Extended Data Fig. 1 | DFT and TDDFT simulation on the energy level of molecular emitters. a, Molecular structures of four different organic emitters. b, The calculated HOMO-LUMO and S1 level of organic molecules relative to the valance band maximum (VBM)-conduction band minimum

(CBM) of lead-bromide matrix. The VBM-CBM value of $[PbBr_4]^{2-}$ was adapted from the literature 39 . **c**, Scheme of the band alignment in organic-inorganic perovskite 2D SL structures including type I, type II and reversed type I.

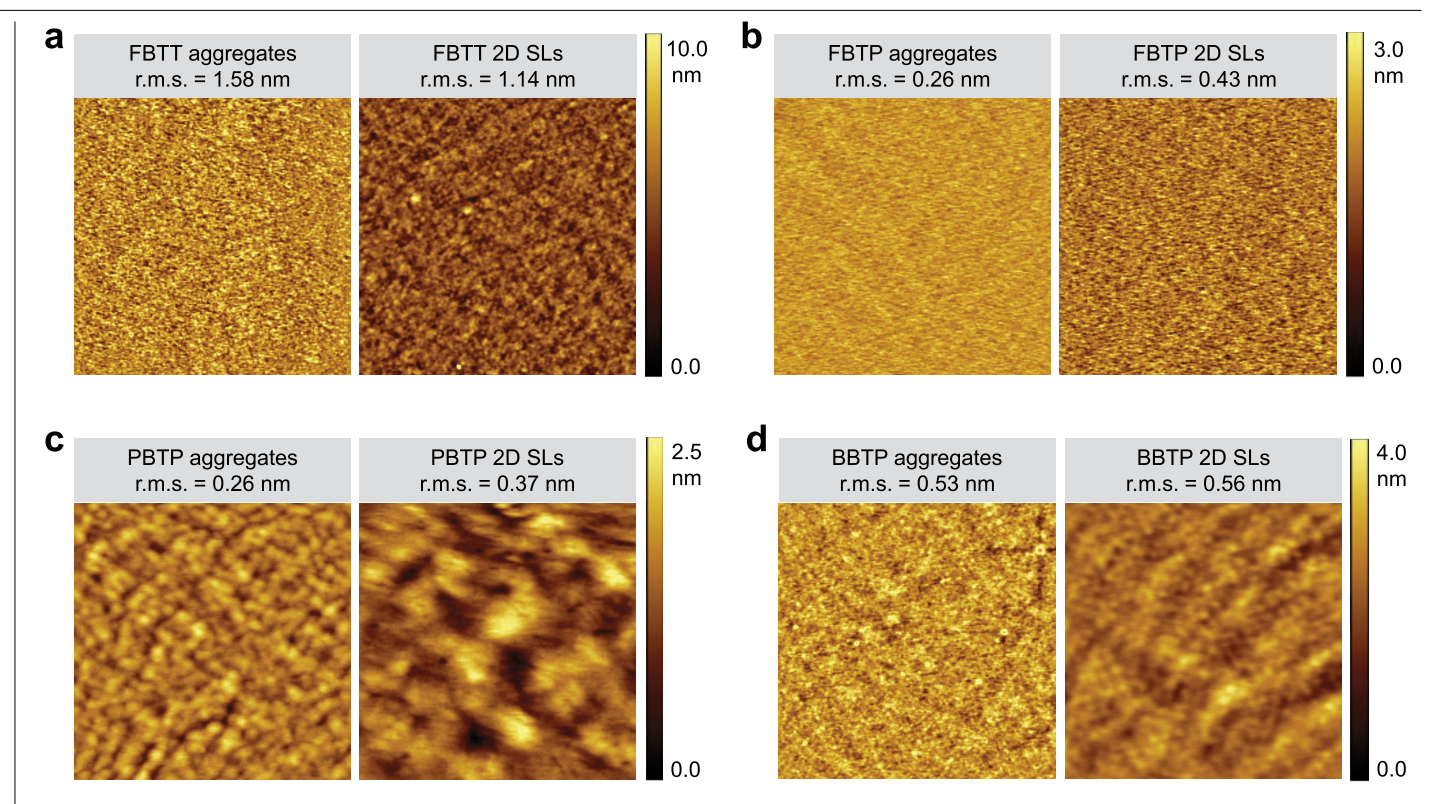


Extended Data Fig. 2 | The extracted azimuthal distribution of GIWAXS intensity for 2D perovskites at a typical q near 0.5 A^{-1} (dashed rings in Fig. 2b,f). a, FBTT 2D SLs. b, FBTP 2D SLs. 0° and 180° correspond to the q_{xy} plane (vertical orientation) and 90° corresponds to the q_z direction (horizontal orientation). For the FBTT sample, it shows a peak scattering intensity of about 2,200 at 90° , which is very similar to that of FBTP (about 2,100). At 0° or 180° , FBTT shows substantial scattering with an intensity of about 410, whereas FBTP has a negligible scattering. Here the orientation factor was defined as the

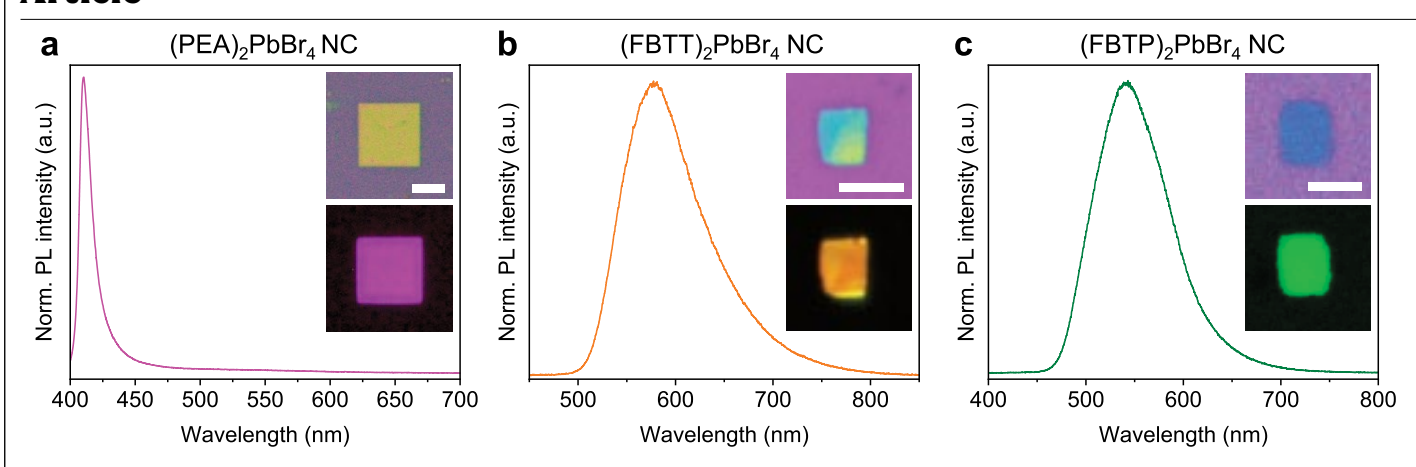
scattering intensity ratio between 0° (180°) and 90°, which yields a value of 0.19 and roughly 0 for FBTT and FBTP, respectively. A greater orientation factor value suggests a preferred orientation along the q_{xy} direction, which corresponds to a vertically oriented $[PbX_4]^{2^-}$ inorganic sublattice relative to the substrate. Therefore, in our scenario, the FBTT sample is dominated by horizontal orientation with a small fraction of vertical orientation, whereas the FBTP sample exhibits an almost perfectly horizontal orientation.



Extended Data Fig. 3 | FBTP emitters confined in 2D SLs with tunable inorganic sublattices. a, PL spectra. b, UV-vis spectra. c, XRD of FBTP-contained 2D SLs with different halide compositions.

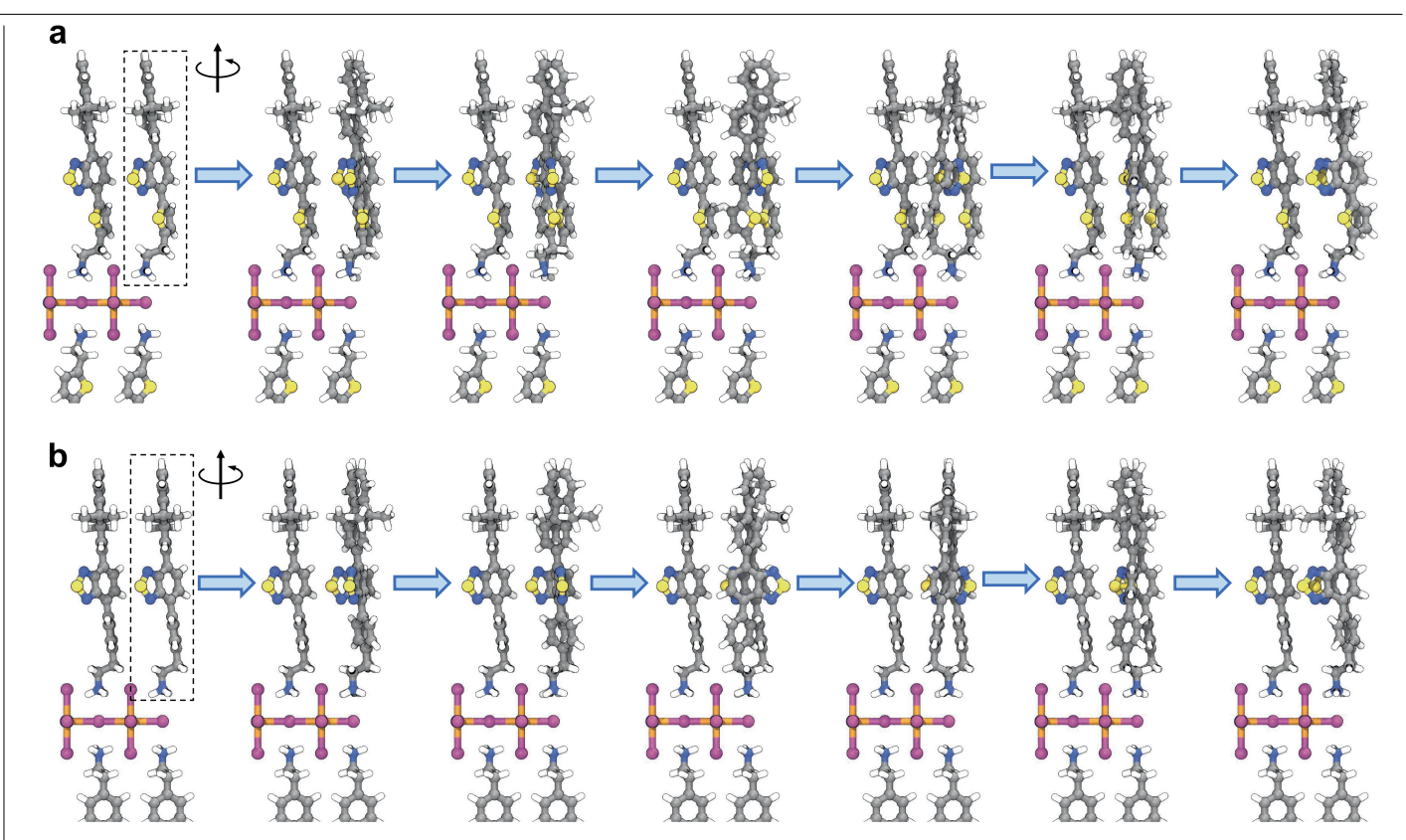


 $\textbf{Extended Data Fig. 4} | \textbf{The atomic force microscopy surface morphology study on both molecular aggregates and 2D perovskites thin-film samples.} \\ \textbf{a}, \textbf{FBTT. b}, \textbf{FBTP. c}, \textbf{PBTP. d}, \textbf{BBTP. The dimensions of all images are 4} \\ \mu \textbf{m} \times 4 \\ \mu \textbf{m}.$

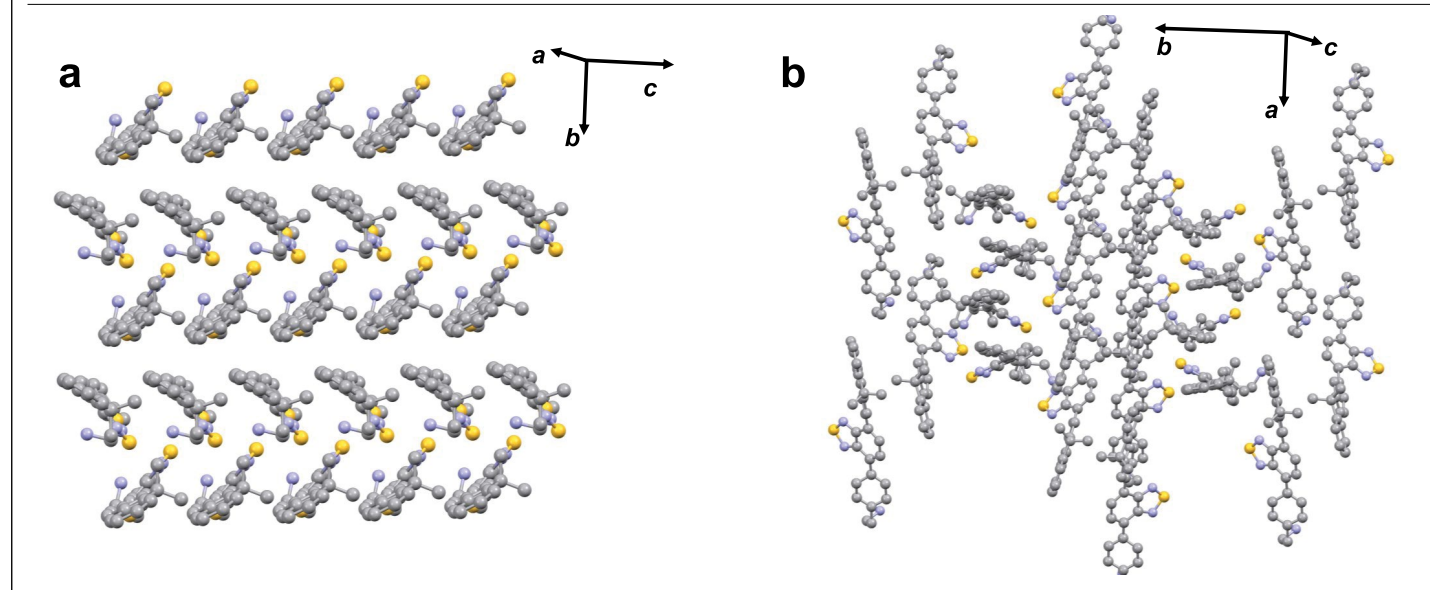


Extended Data Fig. 5 | 2D perovskite nanocrystals and their corresponding PL spectra. a, (PEA) $_2$ PbBr $_4$ nanocrystal. b, (FBTT) $_2$ PbBr $_4$ nanocrystal. c, (FBTP) $_2$ PbBr $_4$ nanocrystal. The scale bars are 5 μ m. The PEA sample shows a square shape with violet emission from the [PbBr $_4$] 2 - inorganic sublattice, which is consistent with the results from the literature 58 , demonstrating the successful growth of single-crystalline (PEA) $_2$ PbBr $_4$ 2D perovskite. By replacing the PEA with FBTT or FBTP, we also obtained rectangular nanocrystals using a similar crystal-growth procedure, implying the formation of single-crystalline

FBTT-based and FBTP-based 2D perovskite nanocrystals. Moreover, FBTT-based and FBTP-based nanocrystals exhibit strong orange and green emission, respectively, which is probably from the organic molecules. By taking a closer look at their PL spectra, we found that the PL peak of the (FBTT) $_2$ PbBr $_4$ nanocrystal is closer to that of FBTT aggregates, whereas the PL peak of the (FBTP) $_2$ PbBr $_4$ nanocrystal closely resembles that of FBTP monomer. These findings align well with our observations from thin-film samples, thus ruling out the influence of crystallinity on different emission properties.

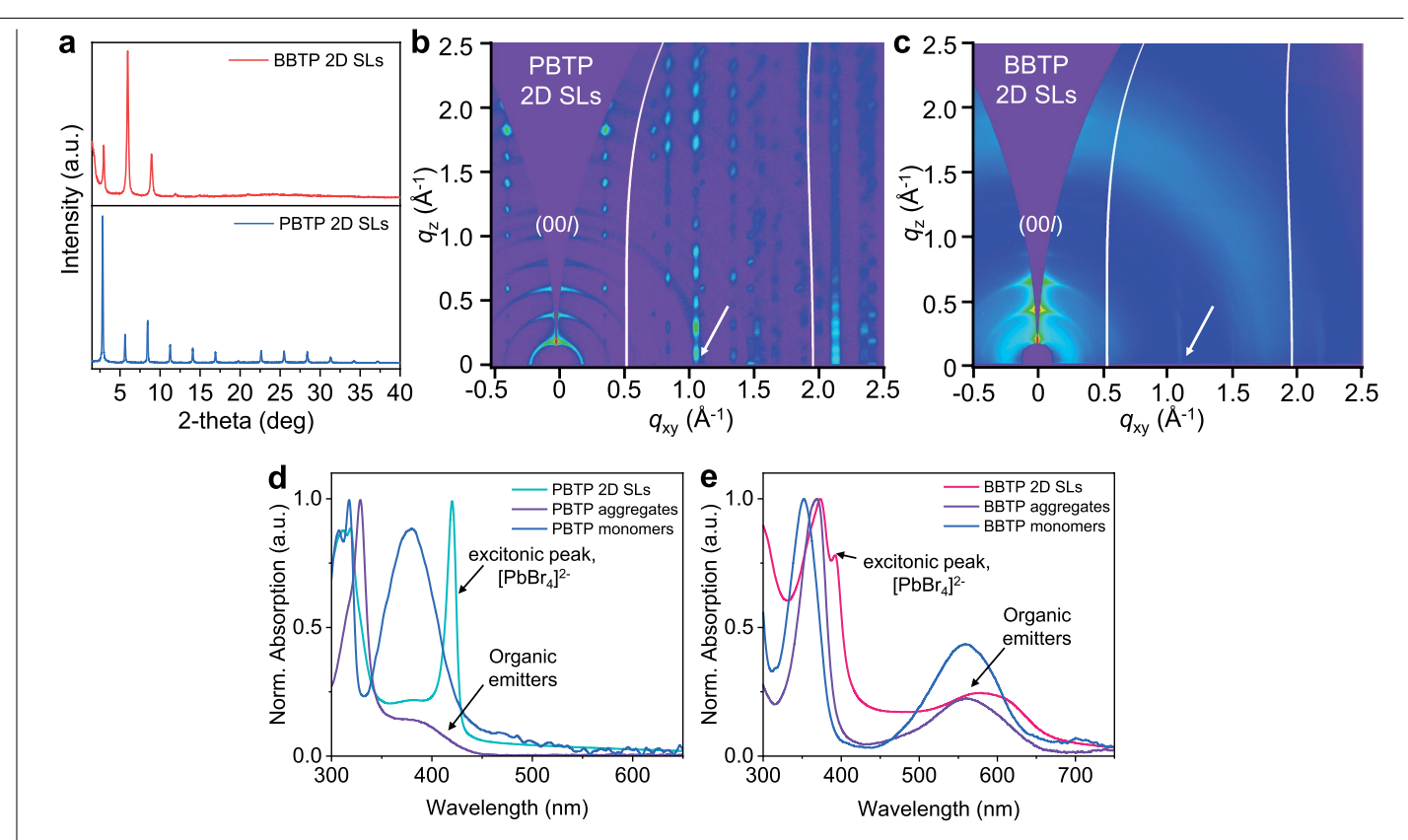


Extended Data Fig. 6 | **Schematic illustration of MD simulations on organic molecules rotation in the perovskite lattice. a**, FBTT-contained 2D SLs. **b**, FBTP-contained 2D SLs. The dashed boxes highlight the molecules under rotation investigation.



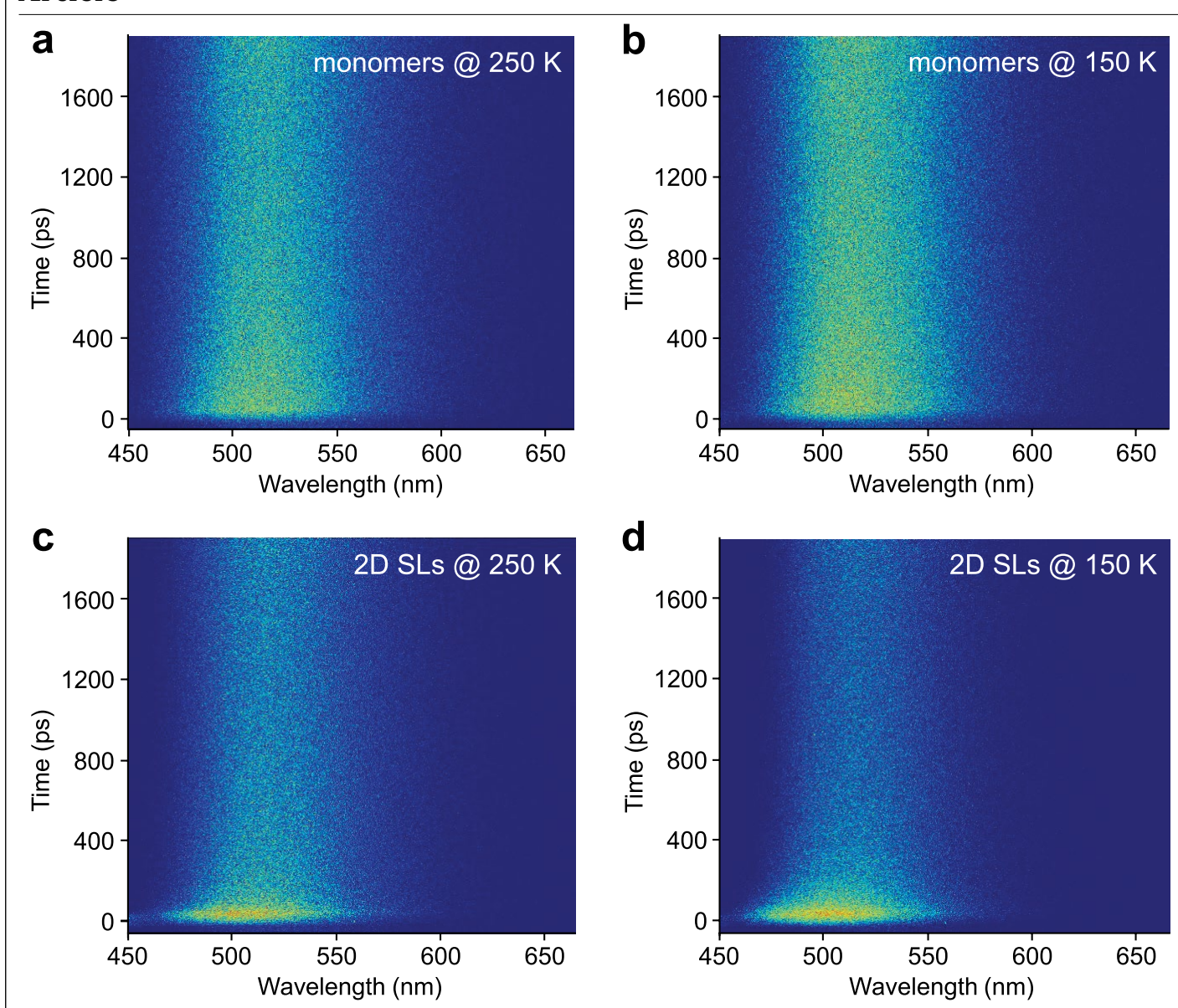
 $\label{eq:continuous} \textbf{Extended Data Fig. 7} | The packing styles of organic molecules within 2D SLs. \\ \textbf{a}, View down the long molecular axis of FBTT molecules in the SLs, which clearly demonstrates a traditional herringbone packing style. \\ \textbf{b}, View down the long$

 $molecular\ axis\ of\ partial\ FBTP\ molecules\ in\ the\ SLs, revealing\ a\ new\ molecular\ packing\ style.\ H\ atoms\ and\ inorganic\ sublattices\ are\ omitted\ for\ clarity.$



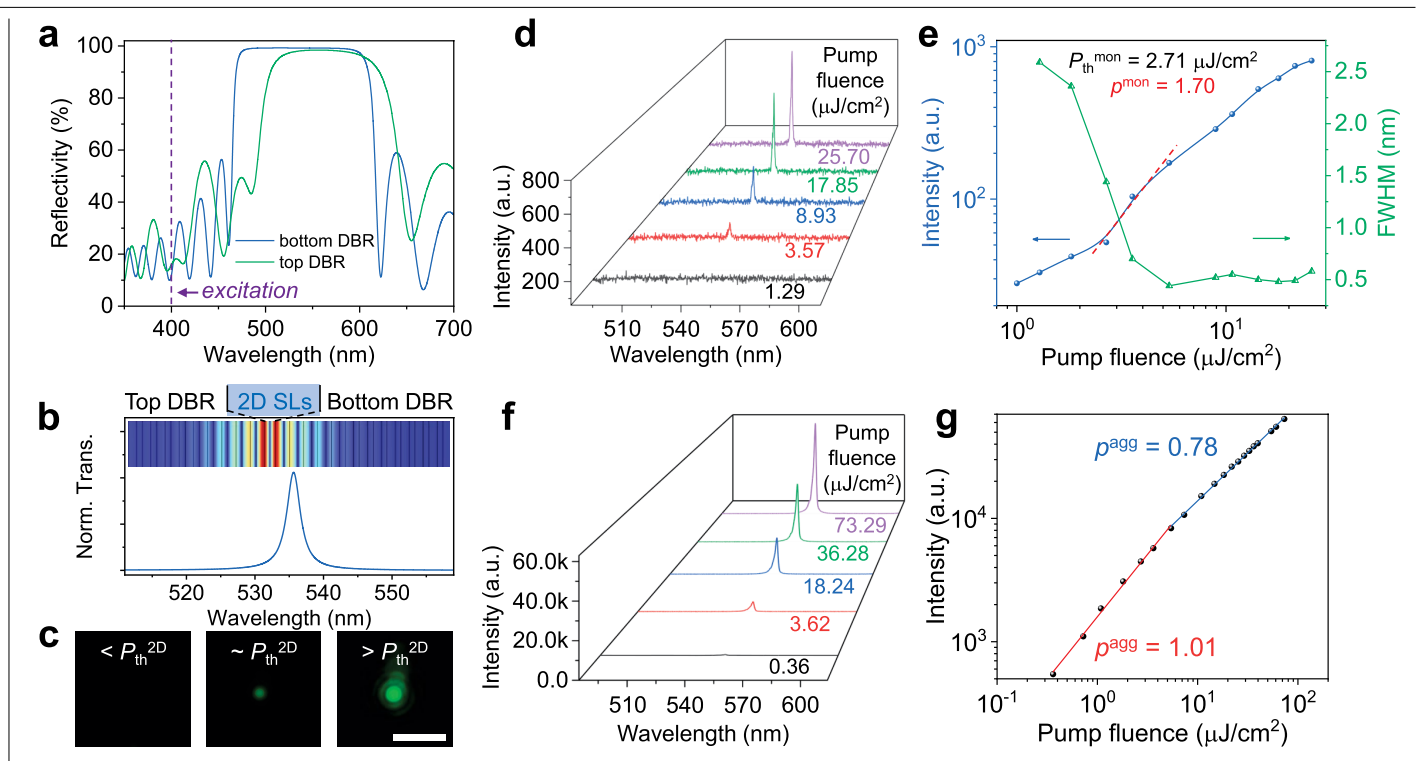
Extended Data Fig. 8 | **Structural characterizations and UV-vis spectra of PBTP-based and BBTP-based thin films.** XRD (**a**) and GIWAXS (**b,c**) patterns for perovskite thin films incorporated with PBTP (**b**) and BBTP (**c**) molecules. XRD and out-of-plane (q_z) GIWAXS patterns help us verify that both PBTP and BBTP have been successfully incorporated into the lead-bromide matrix, forming a layered structure. The in-plane spacing is determined to be 5.98 and 5.76 Å from the q_{xy} direction at 1.05 and 1.09 Å⁻¹ for PBTP and BBTP (similar to the 3D perovskite lattice), respectively, which indicates that the 2D structures

of these organic emitters incorporated 2D SLs. ${\bf d}$, UV-vis spectra of PBTP-doped PMMA (monomers), neat PBTP aggregates and PBTP 2D SLs films. ${\bf e}$, UV-vis spectra of BBTP-doped PMMA (monomers), neat BBTP aggregates and BBTP 2D SLs films. The sharp UV-vis peak around 400 nm and the nearby shoulder peak from 2D SLs films can be indexed to the excitonic peak of perovskites and organic emitters, respectively, further supporting the formation of 2D perovskite SLs.



Extended Data Fig. 9 | Streak-camera results at different temperatures. **a,b,** FBTP monomers at 250 K (**a**) and 150 K (**b**). **c,d,** FBTP 2D SLs at 250 K (**c**) and 150 K (**d**). After carefully examining our FBTP SL sample and its spectroscopic features, we found several reasons to rule out the dispersive energy transfer explanation 64,65 . (1) Our organic emitters in the perovskite lattice are the identical molecules, typically exhibiting homogeneous energy distribution. This is different from the conjugated polymer cases, which show dispersive energy transfer from high-energy sites to low-energy sites owing to the inhomogeneously broadened density of states with different effective conjugation length. (2) Forster-type energy transfer usually requires effective spectral overlap between the absorption and emission spectra. The spectral overlap is minimal in our 2D SL system (Fig. 1g and Supplementary Fig. 5c), which may result in the dispersive energy transport being less effective.

Furthermore, the excitation wavelengths used for time-resolved PL and streak-camera measurements are 447 and 440 nm, respectively, which are near the tail end of the absorption band. This suggests that the dispersive energy transfer is unlikely to play a notable role in the observed bathochromic shift over time. (3) If the dispersive energy transport were occurring in FBTP 2D SLs, the PL spectra would be expected to continuously redshift and reach a stationary energy in a nanosecond timescale. By contrast, our streak-camera results (Fig. 5e and Extended Data Fig. 9c,d) show redshifting only within about 100 ps. More importantly, the final emission state reached in FBTP SLs is exactly the same as that of the FBTP monomer (Fig. 5d and Extended Data Fig. 9a,b). This behaviour implies that the emerging rapid decay at the short-wavelength side originates from the high-energy emission state (that is, locally excited state), rather than from the high-energy fraction of the emitters (broadened density of states).



Extended Data Fig. 10 | Lasing characterization on FBTP monomer and FBTP aggregates. a, Experimentally measured reflectance spectra for DBRs, in which the pump laser was directed into the device from the top DBR to excite the sample, followed by the collection of emission from the same side. The wavelength range of the top DBR with high reflectance (>98%) fully covers the optical gain region of FBTP monomer, 2D SLs and aggregates. b, Simulated transmittance spectra of a 2D SLs-based DBR device, which matches well with the lasing spectra from this device. Inset, electric-field distribution of the 536-nm optical standing wave inside the device. c, PL images of a 2D SLs-based DBR device with pump fluence below, near and above the threshold. Scale bar, 100 μ m.

d, PL spectra evolution of FBTP monomer under different pump fluences. **e**, Corresponding PL intensity against increasing pump fluences in log-log scale, showing a clear 'kink' at a threshold energy density of $2.71\,\mu$ J cm⁻². The superlinear intensity dependence is fitted to a power law x^p with $p^{mon}=1.70$ above the threshold. **f**, PL spectra evolution of FBTP aggregates under different pump fluences. **g**, Corresponding PL intensity against increasing pump fluences in log-log scale, which reveals linear ($p^{agg}=1.01$) and sublinear ($p^{agg}=0.78$) growth across a broad pump fluence range, suggesting the absence of lasing from FBTP aggregates.



	Letian Dou	Corresponding author(s):
--	------------	--------------------------

Lasing Reporting Summary

Nature Research wishes to improve the reproducibility of the work that we publish. This form is intended for publication with all accepted papers reporting claims of lasing and provides structure for consistency and transparency in reporting. Some list items might not apply to an individual manuscript, but all fields must be completed for clarity.

For further information on Nature Research policies, including our data availability policy, see Authors & Referees.

▶ ⊢∨	narım	antal	MACIO	Tn
LA	perim	Cillai	UCSIE	51 L

Please check: are the following details reported in the manuscript?				
1.	Threshold			
	Plots of device output power versus pump power over a wide range of values indicating a clear threshold	X Yes No	Main manuscript: Fig. 5k, Extended Fig. 10d	
2.	Linewidth narrowing			
	Plots of spectral power density for the emission at pump powers below, around, and above the lasing threshold, indicating a clear linewidth narrowing at threshold	X Yes	Main manuscript: Fig. 5k, Extended Fig. 10d	
	Resolution of the spectrometer used to make spectral measurements	X Yes No	Main Manuscript Methods section	
3.	Coherent emission			
	Measurements of the coherence and/or polarization of the emission	X Yes No	Main Manuscript: inset in Fig. 5j; Supplementary Figs. 22 and 23	
4.	Beam spatial profile			
	Image and/or measurement of the spatial shape and profile of the emission, showing a well-defined beam above threshold	X Yes	Main Manuscript: Extended Fig. 10c	
5.	Operating conditions			
	Description of the laser and pumping conditions Continuous-wave, pulsed, temperature of operation	X Yes No	Main Manuscript Methods section	
	Threshold values provided as density values (e.g. W cm $^{\!-2}$ or J cm $^{\!-2}$) taking into account the area of the device	X Yes No	Main manuscript: Fig. 5, Extended Fig. 10	
6.	Alternative explanations			
	Reasoning as to why alternative explanations have been ruled out as responsible for the emission characteristics e.g. amplified spontaneous, directional scattering; modification of fluorescence spectrum by the cavity	X Yes	Main Manuscript: Fig. 5 caption and related discussions; Extended Fig. 10 caption	
7.	Theoretical analysis			
	Theoretical analysis that ensures that the experimental values measured are realistic and reasonable e.g. laser threshold, linewidth, cavity gain-loss, efficiency	X Yes	Main Manuscript: Extended Fig. 10b	
8.	Statistics			
	Number of devices fabricated and tested	Yes No	This work focuses on the the discovery, characterization, and the fundamental understanding of the intriguing behavior of "single-molecule-like aggregates (SMA)" in 2D perovskite lattice.	

nature research
lasing reporting sur
porting
nmn

March 2018

Statistical analysis of the device performance and lifetime (time to failure)	M No	This work focuses on the the discovery, charact understanding of the intriguing behavior of "sin in 2D perovskite lattice.
---	------	--

Demonstration of device is not the purpose of this work.